Cell Stem Cell

Article

Pathogenic *LMNA* variants disrupt cardiac lamina-chromatin interactions and de-repress alternative fate genes

Graphical Abstract

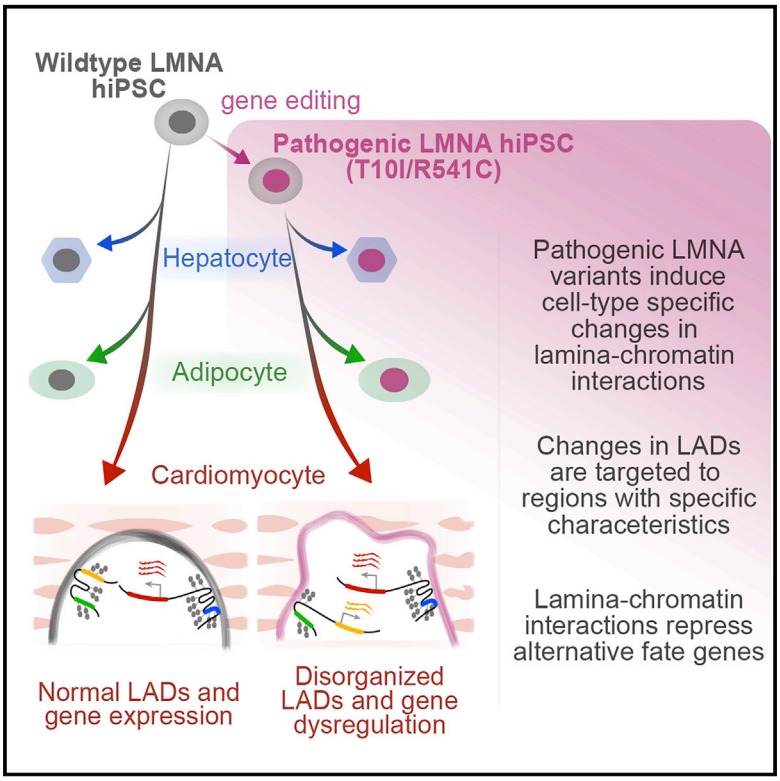

Highlights

- Pathogenic *LMNA* variants disrupt peripheral chromatin in a cell-type-specific manner
- Loss of lamina-bound chromatin occurs in regions with specific characteristics
- Peripheral chromatin organization maintains silencing of alternative fate genes

Authors

Parisha P. Shah, Wenjian Lv, Joshua H. Rhoades, ..., Benjamin L. Prosser, Kiran Musunuru, Rajan Jain

Correspondence

kiranmusunuru@gmail.com (K.M.), jainr@pennmedicine.upenn.edu (R.J.)

In Brief

Shah et al. demonstrate that pathogenic *LMNA* variants affect peripheral chromatin organization in a cell-type-specific manner. Their data suggest that lamina-chromatin interactions guard cellular identity. Pathogenic *LMNA* variants disrupt peripheral chromatin organization and abrogate normal silencing of alternative fate genes in cardiomyocytes.

Shah et al., 2021, Cell Stem Cell *28*, 938–954
May 6, 2021
https://doi.org/10.1016/j.stem.2020.12.016

CellPress

CellPress

Cell Stem Cell

Article

Pathogenic *LMNA* variants disrupt cardiac lamina-chromatin interactions and de-repress alternative fate genes

Parisha P. Shah,[1,2,3,14] Wenjian Lv,[1,3,4,14] Joshua H. Rhoades,[1,2,3,5] Andrey Poleshko,[2] Deepti Abbey,[3,4] Matthew A. Caporizzo,[3,6,7] Ricardo Linares-Saldana,[1,2,3] Julie G. Heffler,[3,6,7] Nazish Sayed,[12] Dilip Thomas,[13] Qiaohong Wang,[1,2,3] Liam J. Stanton,[1,2,3] Kenneth Bedi,[1,3] Michael P. Morley,[1,3,8] Thomas P. Cappola,[1,3] Anjali T. Owens,[1,3] Kenneth B. Margulies,[1,3] David B. Frank,[3,9] Joseph C. Wu,[11] Daniel J. Rader,[3,4] Wenli Yang,[1,3,10] Benjamin L. Prosser,[3,6,7] Kiran Musunuru,[1,3,4,*] and Rajan Jain[1,2,3,10,15,*]

[1]Department of Medicine, University of Pennsylvania, Perelman School of Medicine, Philadelphia, PA 19014, USA
[2]Department of Cell and Developmental Biology, University of Pennsylvania, Perelman School of Medicine, Philadelphia, PA 19014, USA
[3]Penn Cardiovascular Institute, University of Pennsylvania, Perelman School of Medicine, Philadelphia, PA 19014, USA
[4]Department of Genetics, University of Pennsylvania, Perelman School of Medicine, Philadelphia, PA 19014, USA
[5]Institute for Biomedical Informatics, University of Pennsylvania, Perelman School of Medicine, Philadelphia, PA 19014, USA
[6]Department of Physiology, University of Pennsylvania, Perelman School of Medicine, Philadelphia, PA 19014, USA
[7]Pennsylvania Muscle Institute, University of Pennsylvania, Perelman School of Medicine, Philadelphia, PA 19014, USA
[8]Penn Lung Institute, University of Pennsylvania, Perelman School of Medicine, Philadelphia, PA 19014, USA
[9]Department of Pediatrics, University of Pennsylvania, Perelman School of Medicine, Philadelphia, PA 19014, USA
[10]Institute for Regenerative Medicine, University of Pennsylvania, Perelman School of Medicine, Philadelphia, PA 19014, USA
[11]Stanford Cardiovascular Institute, Department of Medicine, Institute for Stem Cell Biology and Regenerative Medicine, Stanford University, Stanford, CA 94305, USA
[12]Stanford Cardiovascular Institute, Department of Surgery, Division of Vascular Surgery, Stanford University, Stanford, CA 94305, USA
[13]Stanford Cardiovascular Institute, Department of Medicine, Stanford University, Stanford, CA 94305, USA
[14]These authors contributed equally
[15]Lead contact
*Correspondence: kiranmusunuru@gmail.com (K.M.), jainr@pennmedicine.upenn.edu (R.J.)
https://doi.org/10.1016/j.stem.2020.12.016

SUMMARY

Pathogenic mutations in LAMIN A/C (LMNA) cause abnormal nuclear structure and laminopathies. These diseases have myriad tissue-specific phenotypes, including dilated cardiomyopathy (DCM), but how LMNA mutations result in tissue-restricted disease phenotypes remains unclear. We introduced LMNA mutations from individuals with DCM into human induced pluripotent stem cells (hiPSCs) and found that hiPSC-derived cardiomyocytes, in contrast to hepatocytes or adipocytes, exhibit aberrant nuclear morphology and specific disruptions in peripheral chromatin. Disrupted regions were enriched for transcriptionally active genes and regions with lower LAMIN B1 contact frequency. The lamina-chromatin interactions disrupted in mutant cardiomyocytes were enriched for genes associated with non-myocyte lineages and correlated with higher expression of those genes. Myocardium from individuals with *LMNA* variants similarly showed aberrant expression of non-myocyte pathways. We propose that the lamina network safeguards cellular identity and that pathogenic *LMNA* variants disrupt peripheral chromatin with specific epigenetic and molecular characteristics, causing misexpression of genes normally expressed in other cell types.

INTRODUCTION

Genome-lamina interactions provide a critical layer of gene regulation, but it remains unclear how these interactions affect cellular identity and disease. The nuclear lamina is a filamentous network of LAMIN A/C (LMNA), LAMIN B1 (LB1), and LAMIN B2 proteins on the inner nuclear surface. *LMNA* mutations result in gross nuclear abnormalities (Burke and Stewart, 2006; Worman and Bonne, 2007) and are the second most common cause of familial dilated cardiomyopathy (DCM) (Taylor et al., 2003). There is a paucity of data reconciling how germline *LMNA* mutations result in tissue-specific phenotypes. *LMNA* mutants can alter normal nuclear rigidity (Houben et al., 2007; Lee et al., 2007), but most tissues express *LMNA*, and soft and stiff tissues are affected by *LMNA* mutations (Burke and Stewart, 2006).

LMNA mutants are implicated in altered gene expression via aberrations in signal transduction or genome organization (Hutchison, 2002; Worman, 2018; Wu et al., 2011). The nuclear lamina associates with large chromatin regions called LAMIN B1-associated domains (LADs) (Guelen et al., 2008). Genes

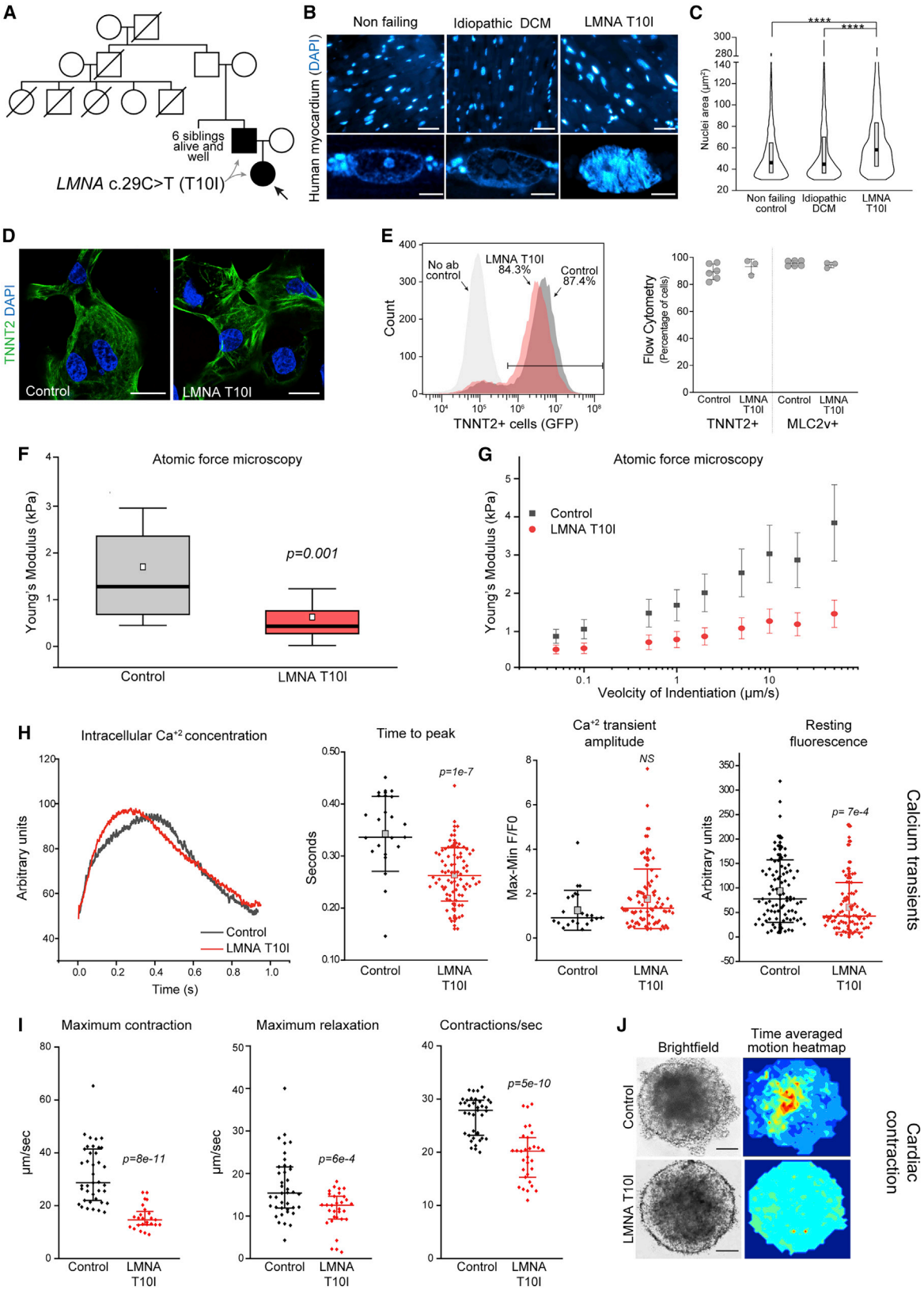

(legend on next page)

in LADs are transcriptionally repressed, and some LADs are repositioned away from or to the lamina during differentiation in a cell-type-specific manner (Meister et al., 2010; Peric-Hupkes et al., 2010). In worms, perinuclear chromatin sequestration contributes to lineage restriction by stabilizing cell fate commitment (Gonzalez-Sandoval et al., 2015). LAD positioning regulates mammalian organogenesis (Peric-Hupkes et al., 2010; Poleshko et al., 2017; Robson et al., 2016), but it is unclear whether compromised LAD organization impairs cell-type-specific gene expression. Pathogenic *LMNA* variants provide an attractive approach to unveil principles underlying the consequences of lamina-genome interactions. To this end, a *C. elegans* mutant lamin muscular dystrophy model displays muscle phenotypes and is rescued by restoring peripheral chromatin organization via loss of a peripheral chromatin tether (Harr et al., 2020).

Because a subset of LADs are cell type specific, mechanisms relevant to tissue-specific disease phenotypes are likely to be influenced by cellular context. This limits the interpretation of studies overexpressing variants or using immortalized cell lines (Mewborn et al., 2010; Perovanovic et al., 2016). Also, only a subset of LADs reposition away from the lamina during differentiation, and often only a portion of a LAD is repositioned (Briand and Collas, 2020). Genomic regions have varying probabilities of re-localization to or from the lamina (Kind et al., 2013, 2015). Thus, different types of peripheral chromatin may exist at the nuclear lamina with distinct mechanisms of establishment or maintenance, function, or genomic features. It is of great interest to understand whether peripheral chromatin is affected uniformly or stochastically by *LMNA* variants. Distinguishing LADs vulnerable to disruption from those that are resistant is vital to understand the mechanism of peripheral chromatin organization and the role of LADs in cellular identity and disease progression.

We introduced a point mutation into one *LMNA* allele in a human induced pluripotent stem cell (hiPSC) line, resulting in a heterozygous T10I LAMIN A mutant, modeled after an individual with laminopathy. Mutant hiPSC-derived cardiomyocytes (hiPSC-CMs) demonstrated impaired physiology, dysmorphic nuclei, and disruption of a specific subset of peripheral chromatin regions characterized by greater gene density, higher expression, and lower LB1 enrichment. hiPSC-CMs carrying a pathogenic *LMNA* R541C mutation showed similar changes. These disruptions were specific to hiPSC-CMs; T10I and R541C hiPSC hepatocytes or hiPSC adipocytes did not demonstrate dysmorphic nuclei or LAD changes. Disrupted hiPSC-CM peripheral chromatin regions were enriched for genes and regulatory regions relevant to non-myocyte cell types, resulting in aberrant expression of genes ordinarily restricted to non-myocyte lineages. These data reveal that a subset of lamina-bound chromatin with definable molecular characteristics is disrupted in disease and may contribute to tissue-specific phenotypes observed in individuals with laminopathy.

RESULTS

LMNA T10I hiPSC-CMs recapitulate human disease phenotypes

Genetic testing of a 33-year-old female with congestive heart failure requiring cardiac transplantation identified a heterozygous *LMNA* T10I (hereafter called T10I) mutation (Figure 1A). The woman's family history was consistent with familial DCM; her father had heart failure requiring cardiac transplantation, and several relatives suffered from heart failure or sudden cardiac death. Explanted myocardium from the proband T10I individual revealed CMs with significantly larger and dysmorphic nuclei compared with myocardium from non-failing hearts or individuals with idiopathic DCM (Figures 1B, 1C, and S1A).

We introduced the T10I mutation via CRISPR-Cas9 into one *LMNA* allele in hiPSCs from an unrelated healthy individual (Figure S1B). hiPSCs that acquired no mutation served as controls. We isolated independent control and T10I clones; assessment of the top 10 Cas9 recognition sites did not identify off-target effects (Figure S1C). We proceeded with two validated clones per genotype and differentiated control and T10I hiPSCs into TNNT2+ CMs (Figure 1D). Flow cytometry across multiple biological replicates confirmed that more than 85% of control and T10I hiPSC-CMs expressed TNNT2 and MLC2v (Figures 1E and S1D; Lian et al., 2013; Zhu et al., 2011). RNA sequencing (RNA-seq) analysis (control, n = 4; T10I, n = 3) confirmed nearly

Figure 1. Establishment of a LMNA T10I model of hiPSC-CMs that mimics individual abnormalities

(A) Pedigree of a family with *LMNA* c29 > T (T10I; proband indicated by an arrow). Multiple family members experienced sudden cardiac death and/or heart failure. Filled shapes are tested individuals (proband, clinical testing; father, research testing).

(B) DAPI staining of myocardium from an individual at the time of orthotopic heart transplantation compared with nonfailing control and idiopathic DCM. Scale bars: 50 μm (top), 5 μm (bottom).

(C) Quantification of CM nucleus size (mean ± SEM, n > 500 nuclei; nonfailing and idiopathic controls are from 4 and 3 patients, respectively; one-way ANOVA Kruskal-Wallis test with Dunn's multiple comparison, ****$p < 0.0001$). A box represents the interquartile range (25^{th}–75^{th} percentile) and a thick line the median.

(D) TNNT2 immunostaining of hiPSC-CMs on day 25. Scale bars, 25 μm.

(E) Representative flow cytometry profiles of day 25 control (dark gray) and T10I (red) hiPSC-CM cultures stained with anti-TNNT2 (unstained, light gray). Quantification of TNNT2 and MLC2v expressing cells showed no significant difference in control and LMNA T10I (independent differentiation per dot, mean ± 1 SD shown).

(F) Atomic force microscopy (AFM) of control and LMNA T10I hiPSC-CMs with an indentation frequency of 1 μm/s (mean, small square box; error bars, 1 SD; large box, median and interquartile range; two-sample two-sided t test with post hoc Bonferroni correction for multiple comparisons).

(G) AFM performed across a range of stimulation rates from single hiPSC-CMs; there is a significant decrease in Young's modulus in T10I. Data are represented as mean ± 1 SD (control, n = 11; LMNA T10I, n = 23).

(H) Transient calcium reporter assays. Right: recording average on left and median and interquartile ranges of individual measurement panels.

(G) and (H) Two-sample two-sided t test with post hoc Bonferroni correction for multiple comparisons.

(I) Cardiac contractile studies from single hiPSC-CMs (median and interquartile range, two-tailed t test).

(F)–(I) Gray, control; red, T10I.

(J) Representative bright-field images and corresponding time-averaged motion heatmaps from motion capture analysis of beating 3D micropatterned CM cultures. Scale bars, 100 μm.

equivalent expression of the mutant and wild-type *LMNA* alleles in T10I hiPSC-CMs (Figure S1E). Immunoblotting confirmed LAMIN A and LAMIN C protein in control and mutant hiPSC-CMs but not undifferentiated cells (noting a reduction in T10I hiPSC-CMs) (Figure S1F). Transfection of IMR90 human fibroblasts with Emerald-tagged LAMIN A or LAMIN A T10I also showed a reduced epitope-tagged LAMIN A signal for T10I compared with the control but equivalent Emerald expression (Figure S1G).

Lamina filaments regulate nuclear and cytoskeletal stiffness (Cho et al., 2019; Lammerding et al., 2004; McKee et al., 2011; Swift et al., 2013; Worman and Bonne, 2007). We measured the elastic and viscoelastic properties of single hiPSC-CMs using atomic force microscopy (AFM; Figures 1F and 1G). T10I hiPSC-CMs had a decreased Young's modulus at physiological rates of mechanical stimulation (2-Hz indentation at 25 V; Figure 1F), impaired elastic properties at low rates of stimulation, and loss of normal viscoelasticity at high rates of stimulation (Figure 1G), consistent with other laminopathy models (Hale et al., 2008; Khatau et al., 2009). A Fluo-4 fluorescence calcium reporter assay demonstrated an unchanged amplitude of spontaneous calcium transients in T10I hiPSC-CMs, but mutants showed a faster time to peak calcium concentration and lower basal fluorescence compared with control cells (Figure 1H). Multiple indices of myocyte contraction performed in single hiPSC-CMs or those grown in 3D micropatterned cultures were reduced in T10I compared with control cells (Figures 1I and 1J). These data indicate that T10I hiPSC-CMs recapitulate physiological abnormalities observed in individuals with *LMNA* mutations and DCM.

Loss of peripheral chromatin organization at the nuclear lamina in LMNA T10I hiPSC-CMs

Nuclear blebbing and rupture are abnormal phenotypes associated with laminopathies (Burke and Stewart, 2006; de Leeuw et al., 2018; Vergnes et al., 2004; Worman and Bonne, 2007). We visualized control and T10I hiPSC-CMs by immunofluorescence and blindly scored nuclei as normal (elliptical), mild defect (slight invagination), or severe defect (multiple invaginations or nuclear rupture/micronuclei). Control hiPSC-CMs demonstrated mostly normal nuclei. T10I hiPSC-CMs showed significantly more mild and severely defective nuclei on days 25 (mid-point) and 45 (later time point) of CM differentiation (Figures 2A and 2B), which was particularly noticeable in multinucleated cells. Severely defective nuclei were also observed in mutants on days 9–10, prior to onset of gross contraction (Figure S1H). Consistent with previous work (Kind et al., 2013; Poleshko et al., 2017; See et al., 2019), histone H3 lysine 9 dimethylated (H3K9me2) chromatin was enriched at the lamina in control cells (Figures 2A–2C), whereas severely defective (Figure 2A) and mildly defective (Figure 2C) T10I hiPSC-CMs showed reduced H3K9me2 enrichment immediately adjacent to the nuclear lamina.

We hypothesized that T10I disrupts peripheral chromatin organization in hiPSC-CMs. LB1 is exclusive to the periphery whereas LAMIN A/C is not (Gesson et al., 2016). LB1-occupied chromatin represents the majority of peripheral LAMIN A/C-bound chromatin (Discussion; Meuleman et al., 2013). We confirmed LB1 antibody specificity for chromatin immunoprecipitation (ChIP; Figure S2A) and performed ChIP sequencing (ChIP-seq) on day 25 control and T10I hiPSC-CMs (Figure 2D; Table S1). We merged biological replicates with high reproducibility (control, n = 3; T10I, n = 4) (Figure S2E) and identified LAMIN B1-associated domains (LADs) using Enriched Domain Detector (EDD) (Figure 2D; Lund et al., 2014). In control and T10I hiPSC-CMs, we identified 750–800 LADs (Table S1) occupying ~25% of the genome. Approximately 18.5% of LAD coverage was shared (shared LADs), with ~6.7% of control LAD coverage lost in T10I cells (control-only LADs) and ~6.0% of T10I LAD coverage gained and unique to T10I cells (T10I-only LADs) (Figure 2E; Table S1). Parallel trends were observed in day 45 control and T10I hiPSC-CM ChIP-seq (control and T10I, n = 4; Figures S2B and S2C; Table S1).

RNA-seq on day 25 (Table S2) confirmed that genes in control and T10I hiPSC-CM LADs are significantly repressed relative to non-LAD genes (Figure 2F). To determine the consistency of pathologic *LMNA* variants, we established a second set of hiPSC lines harboring the mutation *LMNA* R541C from an individual (hereafter called R541C; Figure S2D). The R541C individual also presented with DCM (explanted myocardium was not available for further analysis). We validated independent clones via sequencing for off-target effects (Figure S2E) and proceeded with two validated clones. Flow cytometry indicated consistent and efficient differentiation (Figure S2F). RNA-seq on day 25 (control and R541C, n = 4; Table S2) confirmed equal transcription from mutant and wild-type *LMNA* alleles in the heterozygous mutants (Figure S2G), and LAMIN A and C proteins were confirmed by immunoblotting (Figure S2H). Validated control lines were generated during construction of mutants and confirmed to not harbor T10I/R541C mutations. We combined datasets from the control lines to create a union control for subsequent analyses.

Similar to T10I, AFM of R541C hiPSC-CMs showed impaired elastic properties at physiologic rates of mechanical stimulation (2 Hz) and decreased viscoelastic response to a range of stimulations (Figures S3A and S3B). R541C hiPSC-CMs also demonstrated a significantly faster time to peak cytosolic calcium concentration compared with control cells and slightly lower basal calcium concentrations (Figure S3C). R541C hiPSC-CMs showed a significant subset of cells with mild and severe nuclear morphology defects and disruption of H3K9me2 at the nuclear periphery (Figure S3D). We defined LADs (Table S1) from LB1 ChIP-seq in R541C hiPSC-CMs (n = 3; Figure S3E) and confirmed that LAD genes were relatively less expressed compared with non-LAD genes (Figure S3F; Table S2). Principal-component analysis (PCA) of the hiPSC-CM ChIP-seq data showed distinct separation of T10I and R541C LADs from control LADs (Figure S3G).

Domains of H3K9me2-modified chromatin (H3K9 dimethylated domains [KDDs]) closely mirror LADs under physiological conditions (Poleshko et al., 2017). We performed H3K9me2 ChIP-seq in control, T10I, and R541C hiPSC-CMs and defined KDDs (control and T10I, n = 4; R541C, n = 3; Figure S3A; Table S1). As with LADs, genes in KDDs were relatively less expressed compared with genes outside of KDDs (Figure S4B). PCA of KDDs and LADs from all hiPSC-CM datasets (Figure 2G) showed separation of mutant LADs and KDDs from controls. LADs from both mutants clustered together, suggesting a consistent LAD

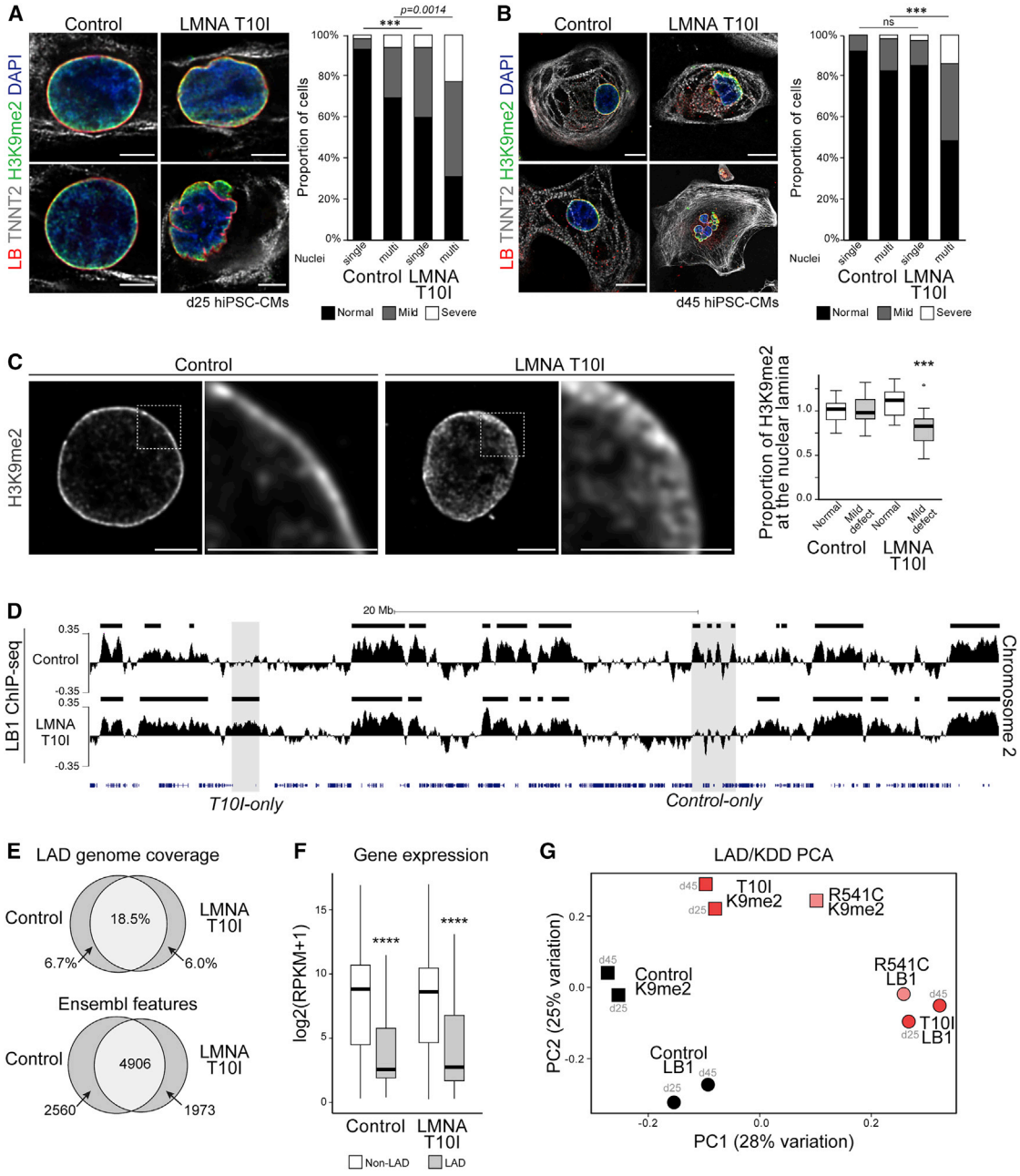

Figure 2. Loss of genome organization at the nuclear lamina in LMNA T10I and R541C human hiPSC-CMs

(A and B) Immunofluorescence of representative control and LMNA T10I hiPSC-CMs on days 25 (A) and 45 (B) stained for LB (red), TNNT2 (gray), and H3K9me2 (red) with accompanying scoring of morphology (n > 30 cells per condition; day 25: 3 × 2 χ^2 single nuclei to single nuclei = 44.66 with 2 degrees of freedom, 3 × 2 χ^2 multi-nuclei to multi-nuclei = 13.11 with 2 degrees of freedom; day 45: 3 × 2 χ^2 multi-nuclei to multi-nuclei = 18.53 with 2 degrees of freedom; ***p < 0.001). Scale bars: 5 μm (A), 10 μm (B).

(C) Immunofluorescence of the indicated hiPSC-CMs (day 45) shows a decreased proportion of H3K9me2 (gray) at lamina in mutants (scale bars, 5 μm; one-way ANOVA Kruskal-Wallis test with Dunn's multiple comparison; p = 0.0004, 0.0004, < 0.0001 of the last bar compared with the three adjacent bars, respectively; boxes indicate median and interquartile range with Tukey whiskers).

(D) LB1 ChIP-seq of control and T10I hiPSC-CMs (day 25, chromosome 2, ~135–195 Mb); gray boxes show LADs in control-only or T10I-only. Black bars, EDD-defined LADs.

(E) Genome coverage (top) and Ensembl feature representation (bottom) in control and LMNA T10I LADs (day 25).

(F) Expression of protein-coding genes within and outside of LADs. The boxplot indicates median and interquartile range with upper and lower hinges representing 25th and 75th percentiles, respectively; whiskers denote 1.5× interquartile range (Kruskal-Wallis rank-summed test; ****p < 0.0001 compared with the respective non-LAD).

(G) PCA of LB1 (circle) and H3K9me2 (square) occupancy across control (black), LMNA T10I (red) and LMNA R541C (pink) hiPSC-CMs. PC1, genotype; PC2, ChIP condition.

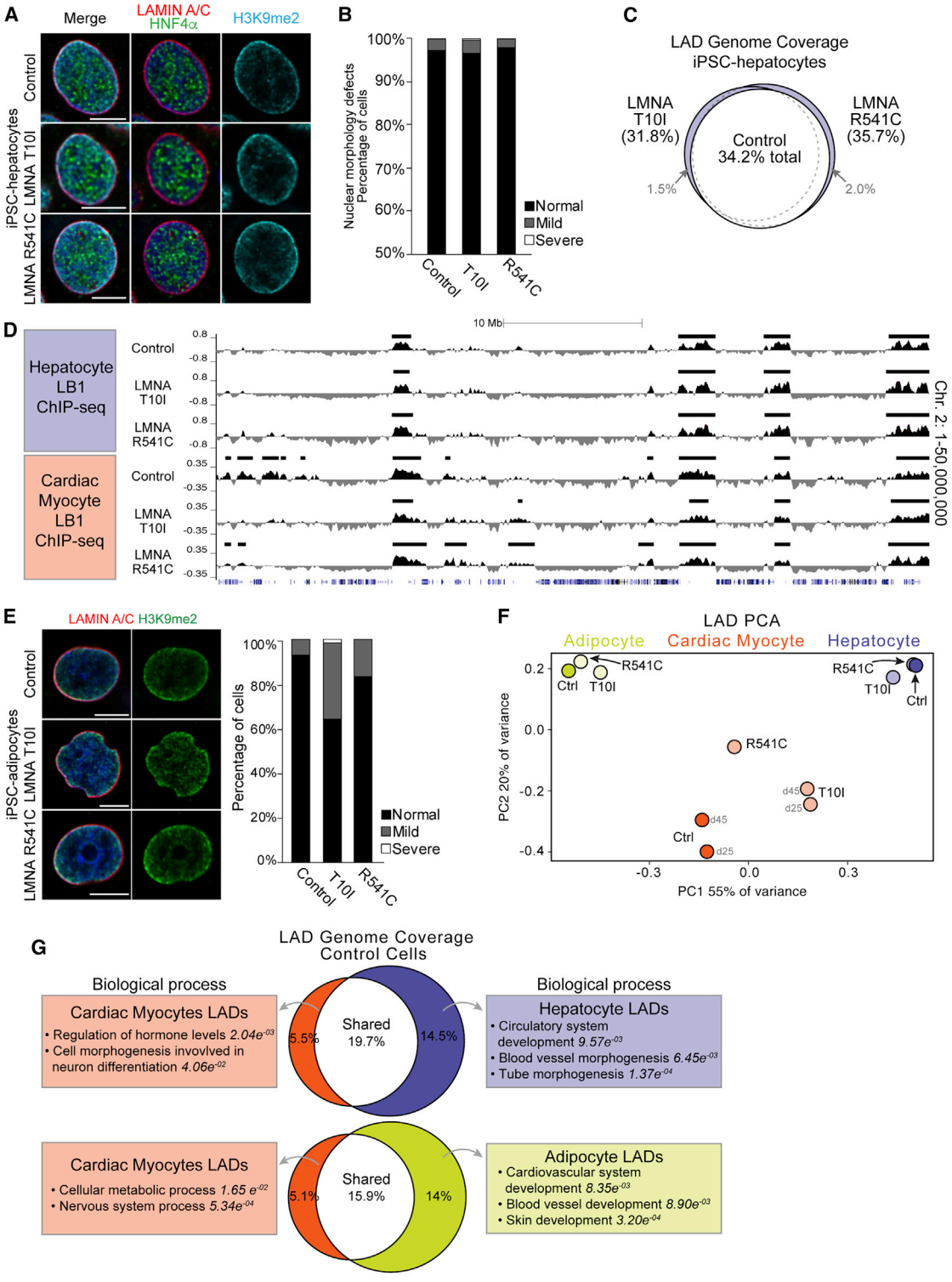

Figure 3. Changes in peripheral chromatin induced by *LMNA* variants are specific to hiPSC-CMs

(A) Immunostaining of representative day 23 control and mutant hiPSC-heps with the indicated antibodies. Scale bars, 5 μm.

(B) Double-blind quantification of nuclear morphology of the indicated hiPSC-heps. (T10I versus control: 3×2 $\chi^2 = 0.4485$, $p = 0.799098$; R541C versus control: 3×2 $\chi^2 = 0.5211$, $p = 0.770646$; $n > 500$ cells per genotype).

(C) 3-way Venn diagram showing LAD genome coverage overlap between control (white) and T10I and R541C (blue) hiPSC-heps.

(D) Comparison of LB1 genome occupancy across a 50-Mb region of chromosome 2 in hiPSC-heps (top) and hiPSC-CMs (bottom).

(legend continued on next page)

defect. PCA also showed greater separation between LB1 and H3K9me2 in mutant compared with control hiPSC-CMs, suggesting that LAD/KDD co-occupancy may be reduced in the mutants. Because individual replicate data were combined for genomic analyses (unless indicated otherwise), any biases arising from differentiation or ChIP variability are attenuated in the final data. Collectively, these data establish that two different *LMNA* variants result in grossly abnormal nuclei and disruption of chromatin-lamina interactions, as defined by LB1 or H3K9me2 occupancy in hiPSC-CMs.

LADs discriminate cell types, and changes in T10I and R541C peripheral chromatin are restricted to hiPSC-CMs

Laminopathy phenotypes are often tissue restricted. Thus, we assessed T10I and R541C in different cell types. We differentiated control, T10I, and R541C hiPSCs into hepatocytes (hiPSC-heps) (Cai et al., 2008) and confirmed ALBUMIN and LAMIN A/C protein on day 23 (Figures S4C and S4D). Clinical laminopathy phenotypes have been observed in hepatocytes, but they are less prevalent than cardiac phenotypes (Brady et al., 2018; Rankin and Ellard, 2006). The T10I individual presented with steatohepatitis with unclear etiology (Hussain et al., 2018), but control, T10I, and R541C hiPSC-heps showed no clear differences in nuclear morphology, H3K9me2 staining, or cellular stiffness (Figures 3A, 3B, S4E, and S4F). We performed LB1 and H3K9me2 ChIP-seq and defined LADs and KDDs in control, T10I, and R541C hiPSC-heps (each genotype, n = 2 replicates/ChIP condition; Figures 3C, 3D, and S4G; Table S1). PCA and visual inspection of the data showed close clustering of mutant LADs and KDDs with control hiPSC-hep LADs and KDDs unlike in hiPSC-CMs (Figures 3D and S4H).

We also differentiated hiPSCs into adipocytes (hiPSC-adips; Su et al., 2018) and confirmed LAMIN A/C protein (Figure S4I) and comparable lipid accumulation by BODIPY staining (Merrick et al., 2019) across all genotypes (Figure S4J). A portion of T10I hiPSC-adips had more mildly defective nuclei than control cells but few severely defective nuclei, unlike hiPSC-CMs (compare Figures 3E, S4J, and S5A with Figures 2A, 2B, and S3D). AFM showed reduced elasticity of T10I compared with control hiPSC-adips (Figure S4K), but the differences were minor compared with hiPSC-CMs (Figure S4L). hiPSC-adip LADs and KDDs (Table S1), defined from LB1 and H3K9me2 ChIP-seq (n = 2/genotype), also showed minor changes (Figures S5A and S5B; Table S1). LAD PCA (Figure 3F) or LAD/KDD PCA (Figure S5C) of all three cell types showed separation of mutant hiPSC-CM LADs or KDDs from controls, whereas mutant hiPSC-adips or hiPSC-heps showed minimal differences from cell-type controls (Figures 3F and S5C). Thus, T10I and R541C LADs and KDDs are preferentially disrupted in hiPSC-CMs.

PCA also showed separation of control hiPSC-CMs, -heps, and -adips, indicating clear cell-type-specific differences in LADs and KDDs. Previous studies in a single progressive lineage (Peric-Hupkes et al., 2010) have indicated that a subset of LADs are cell type specific, but relatively few comparisons have been made between LADs of cell types across different lineages. Therefore, we performed pairwise Gene Ontology comparisons of genes in cell-type-specific LADs (e.g., control hiPSC-CMs versus control hiPSC-heps or -adips) (Figure 3G). We identified "opposite" cell type signatures within each comparison; a subset of categories is shown in Figure 3G. LADs unique to hiPSC-heps are enriched for muscle biology and cardiac development genes versus hormone regulation and hormone metabolism genes in hiPSC-CM-only LADs (Table S3). Unique hiPSC-adip LADs are enriched for skeletal system morphogenesis and cardiovascular development genes versus cellular metabolism and metabolic processing genes in hiPSC-CM-only LADs (Table S3). These data reveal cell-type-specific organization of LADs and suggest that lamina-chromatin interactions are linked to identity.

LMNA T10I and R541C affect a subset of lamina-associated chromatin with specific molecular and epigenetic features

Our data indicated that a subset of lamina-chromatin interactions is affected by the *LMNA* variants in hiPSC-CMs. We hypothesized that a molecular signature would distinguish shared LADs (which do not change between control and mutant) versus control-only LADs (which are present in control but not T10I hiPSC-CMs) or T10I-only LADs (which are present in T10I but not control hiPSC-CMs). Recent studies have identified different types of LADs in immortalized cell lines based on molecular features (Leemans et al., 2019; Paulsen et al., 2019; Zullo et al., 2012), but it is not known whether LAD subtypes behave similarly in primary cells or are differentially dysregulated in disease.

We quantified four molecular and epigenetic features—LB1 contact frequency, gene density, gene expression, and genomic location—across control and mutant hiPSC-CMs LADs. First, we ranked all control hiPSC-CMs LADs (i.e., all shared and control-only LADs) in deciles from least to greatest LB1 contact frequency (Figure 4A), as measured by LB1 ChIP-seq enrichment. In a stepwise fashion, deciles with the highest LB1 contact frequency were enriched for shared LADs, and deciles with the lowest LB1 contact frequency were enriched for control-only LADs (Figure 4B). In a reciprocal approach, we compared length-normalized LB1 contact frequency across regions defined as shared LADs, control-only LADs, and T10I-only LADs in hiPSC-CMs. Of regions defined as LADs in control cells, control-only LADs demonstrated the lowest LB1 contact

(E) Immunostaining of representative control and mutant hiPSC-adips with the indicated antibodies. Scale bars, 5 μm. Right: double-blind quantification of nuclear morphology in control and mutant hiPSC-adips. n > 300 cells per genotype (T10I versus control: 3 × 2 χ^2 = 29.3092, p < 0.0001; R541C versus control: 3 × 2 χ^2 = 6.1111, p = 0.047097).

(F) PCA of LB1 datasets across all three cell types. Independent of genotype, LADs from different cell types show distinct clustering. Control and mutant hiPSC-heps (blue) and -adips (green) cluster together. Mutant hiPSC-CMs are distinctly clustered from the control (orange).

(G) Comparison of LADs from control hiPSC-CMs (orange) to control hiPSC-heps (blue) and control hiPSC-CMs to control hiPSC-adips (green). Genes relevant to alternative cellular identities are enriched in cell-type-specific LADs. Gene Ontology shows enrichment of genes/categories relevant to the opposite cell type per pairwise comparison; selected categories are shown.

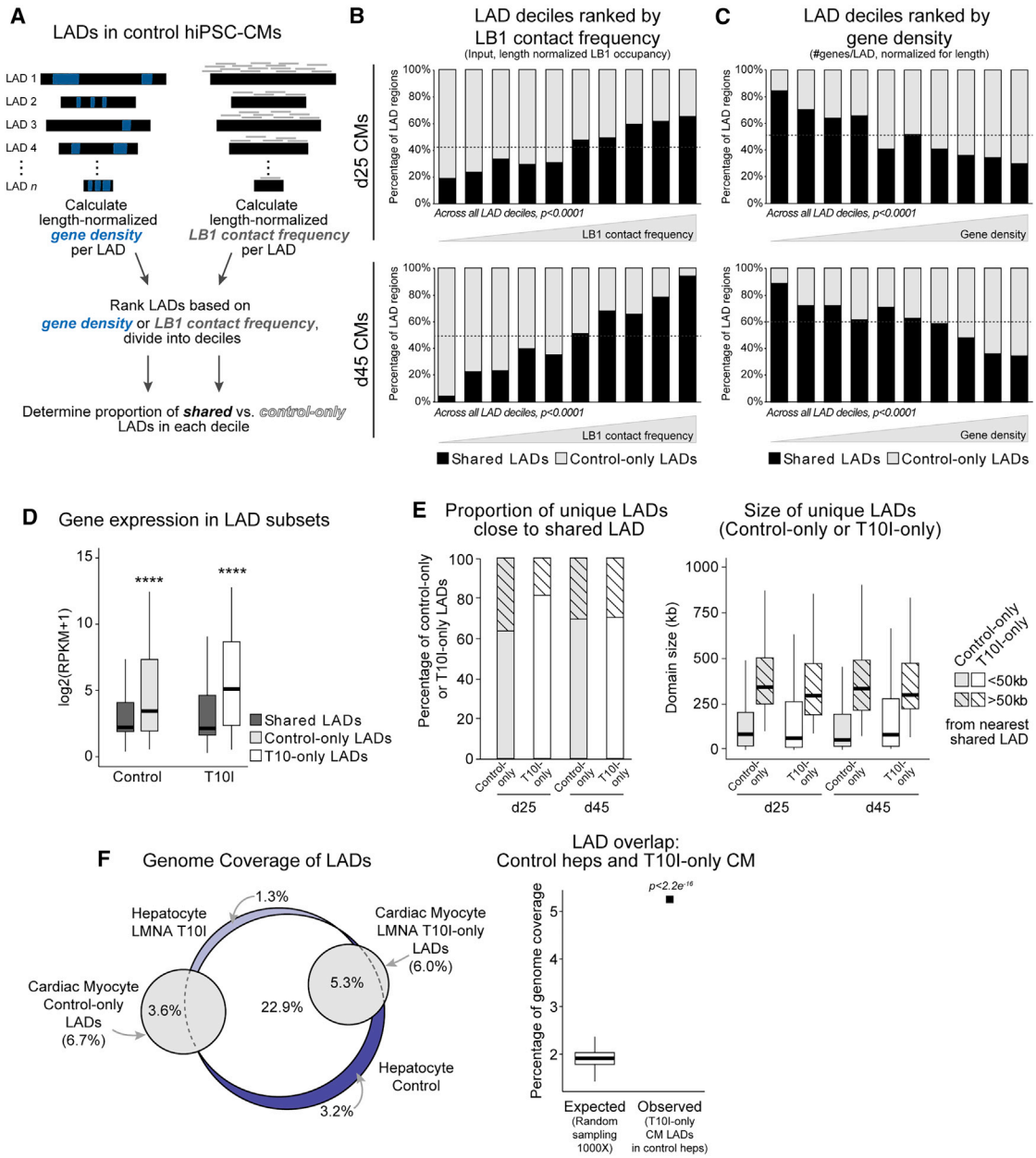

Figure 4. A specific subset of lamina-associated chromatin is affected by LMNA T10I hiPSC-CMs

(A) Schematic of gene density and LB1 contact frequency calculations in control hiPSC-CM LADs.

(B and C) LB1 contact frequency (B) and gene density index (C) of shared LADs (black) and control-only LADs (gray) separated into deciles of increasing LB1frequency or gene density across increasing control day 25 (top) and day 45 (bottom). Dotted lines indicate percentages of LADs shared in each analysis. In (B), n = 1,201 and 1,333 total LAD regions for day 25 and day 45, respectively. In (C), gene density analysis includes LADs with at least one gene; n = 640 and 753 LAD regions for day 25 and day 45, respectively. Control-only LADs are significantly enriched for lower LB1 contact frequency and higher gene density. In (B), 2×10 $\chi^2 = 72.462$ and 195.958 with 9 degrees of freedom, top and bottom, respectively. In (C), 2×10 $\chi^2 = 37.610$ and 34.439 with 9 degrees of freedom, top and bottom, respectively.

(D) Expression of genes in shared versus control-only LADs in control hiPSC-CMs (left). Expression of genes in shared versus T10I-only LAD regions in T10I hiPSC-CMs (right; Kruskal-Wallis rank-summed test with Conover test; ****$p < 0.0001$ to the respective shared LAD regions).

(E) Measure of genomic distance for control-only (gray) and T10I-only (white) LADs to the nearest shared LAD (left). The majority of control-only and T10I-only LADs are within 50 kb (open squares) of the end of a shared LAD. Shown is the size of control-only and T10I-only LADs near shared LADs versus control-only and T10I-only LADs more than 50 kb away (cross-hatched squares) from shared LADs (right).

Boxplots in (D) and (E) indicate median and interquartile range (upper and lower hinges represent the 25th and 75th percentiles, respectively), and whiskers denote 1.5× interquartile range.

(legend continued on next page)

frequency, whereas T10I-only LADs demonstrated the lowest LB1 contact frequency of regions defined as LADs in T10I cells (Figure S5D). Comparing LB1 contact frequency of control versus R541C hiPSC-CM LADs demonstrated a similar relationship (Figure S5D). Thus, control-only and T10I- or R541C-only LADs (i.e., LADs present in only in control or mutant hiPSC-CMs, respectively) have an LB1 signature distinct from shared LADs.

Next we considered whether the *LMNA* variants affected LADs with more genes. We ranked all control hiPSC-CM LADs in deciles based on gene density (Figure 4A) and identified the proportion of shared LADs or control-only LADs per decile. In a stepwise inverse relationship, deciles of LADs with the highest gene density were enriched for control-only LADs, whereas deciles with low-gene-density LADs were enriched for shared LADs (Figure 4C). In a reciprocal approach, we quantified the length-normalized number of genes across each shared LAD, control-only LAD, and T10I-only LAD in hiPSC-CMs (Figure S5E). Control-only LADs demonstrated the highest gene density in control hiPSC-CMs, whereas T10I-only LADs demonstrated the highest gene density in T10I hiPSC-CMs. Shared LADs were relatively gene depleted. R541C hiPSC-CM LAD gene density assessments demonstrated similar relationships (Figure S5E). Thus, we observed that control-only and T10I/R541C-only LADs have a higher gene density than shared LADs.

We next compared expression of shared LAD versus control-only LAD genes in control hiPSC-CMs and expression of shared LAD versus T10I-only LAD genes in T10I hiPSC-CMs. In control and T10I hiPSC-CMs, genes in shared LADs demonstrated lower expression levels compared with genes in control-only LADs or T10I-only LADs, respectively (Figure 4D). We also observed this distinction when considering genes in control and R541C hiPSC-CM shared LADs versus control-only or R541C-only LADs (Figure S5F). These assessments indicate that LAD regions unique to controls or mutants are characterized by higher gene expression, even under the control condition, further distinguishing control-only and T10I/R541C-only LADs from shared LADs.

We hypothesized that LAD aberrations occur near shared LADs rather than being dispersed randomly throughout the genome. We calculated the proportion of control-only or T10I-only LADs within 50 kb (10% of the median size of hiPSC-CM LADs; Table S1) of a shared LAD. The majority of control-only LADs were near a shared LAD in control hiPSC-CMs, and a majority of T10I-only LADs were near a shared LAD in T10I hiPSC-CMs (Figure 4E). Control-only or T10I-only LADs near shared LADs were also smaller than control-only or T10I-only LADs found more than 50 kb away from a shared LAD (Figure 4E). Thus, location is a further distinguishing characteristic of regions affected by the *LMNA* mutants, underscoring the non-stochastic nature of affected LAD regions.

Finally, we asked whether T10I-only and R541C-only LADs were truly unique. We reasoned that if the *LMNA* variants result in stochastic LAD formation in mutant hiPSC-CMs, then there would be limited overlap between these mutant-only LADs in hiPSC-CMs and LADs of another cell type. We found that the vast majority of T10I-only LADs (in terms of genome coverage) overlapped with LADs in control or T10I hiPSC-heps (5.3% of 6.0%; Figure 4F). A permutation analysis (1,000× random sampling) of the same number and size of T10I-only hiPSC-CM LADs demonstrated that this significant overlap was unlikely to have occurred by chance. We found a similar phenomenon for R541C-only LADs in hiPSC-CMs compared with control/R541C hiPSC-heps (Figure S5G).

Collectively, these assessments indicated that *LMNA* T10I and R541C affect specific LAD regions in hiPSC-CMs. Unsupervised gene density and LB1 contact frequency assessments discriminate disrupted LADs (i.e., control-only) versus those that are unaffected (i.e., shared LADs). More broadly, these analyses revealed that only a specific subset of peripheral chromatin is affected in T10I and R541C; LADs with higher gene density, lower LB1 contact frequency, higher expression, and positioning close to shared LADs are preferentially affected by *LMNA* variants. The consistency of these changes across time points and mutations, the molecular signature, and the graded effects strongly suggest that the LB1-chromatin disruptions induced by pathologic *LMNA* variants are specific and targeted.

T10I and R541C result in loss of lamina association of non-myocyte lineage pathway genes and their misexpression

LADs in differentiated cells harbor progenitor and alternative fate genes (Peric-Hupkes and van Steensel, 2010; Poleshko et al., 2017). We hypothesized that peripheral chromatin with genes relevant to non-myocyte cell types are affected in mutant hiPSC-CMs. First we identified lamina-associated regions that are uniquely enriched in LB1 occupancy consistently across the individual replicates in control or T10I hiPSC-CMs but not both (STAR methods; Table S4) and assessed the biological enrichment of genes and regulatory elements in these regions using Genomic Regions of Enrichment Annotations Tool (GREAT) (McLean et al., 2010). This analysis revealed enrichment of non-cardiac cell type regulatory regions and genes, particularly neurobiology (Figure 5A; Table S4). Control-only hiPSC-CM LADs on days 25 and 45 also showed enrichment for genes related to neurobiology (Figure S6A; Table S4). Accordingly, neuronal-related LAD genes demonstrated a nearly 2-fold greater reduction in LB1 occupancy compared to the LB1 occupancy change of non-neuronal LAD genes in T10I hiPSC-CMs (Figure 5B). Consistent with the LAD analyses presented in Figure 4, neuronal LAD genes had lower baseline LB1 occupancy than non-neuronal genes. The LB1 occupancy assessments circumvent challenges arising from the binary definition of LADs/non-LADs. It is known that the majority of the genome has a varying probability of being lamina-associated (Briand and Collas, 2020; Kind et al., 2013); the LB1 occupancy analyses reflect this probability. Non-myocyte lineage-specific genes,

(F) Genome occupancy of LADs in control (dark blue) and T10I (light blue) hiPSC-heps and control-only and T10I-only LADs from day 25 hiPSC-CMs; shared overlap is shown in white. Control-only hiPSC-CM LADs are mostly unique to hiPSC-CMs, whereas T10I-only CM LADs overlap with hiPSC-hep LADs. The boxplot shows significant lower overlap of 1,000 shuffled "test" LAD regions (same number/size of each T10I-only LAD), with control hiPSC-hep LADs compared with the observed overlap (two-tailed one-sample t test).

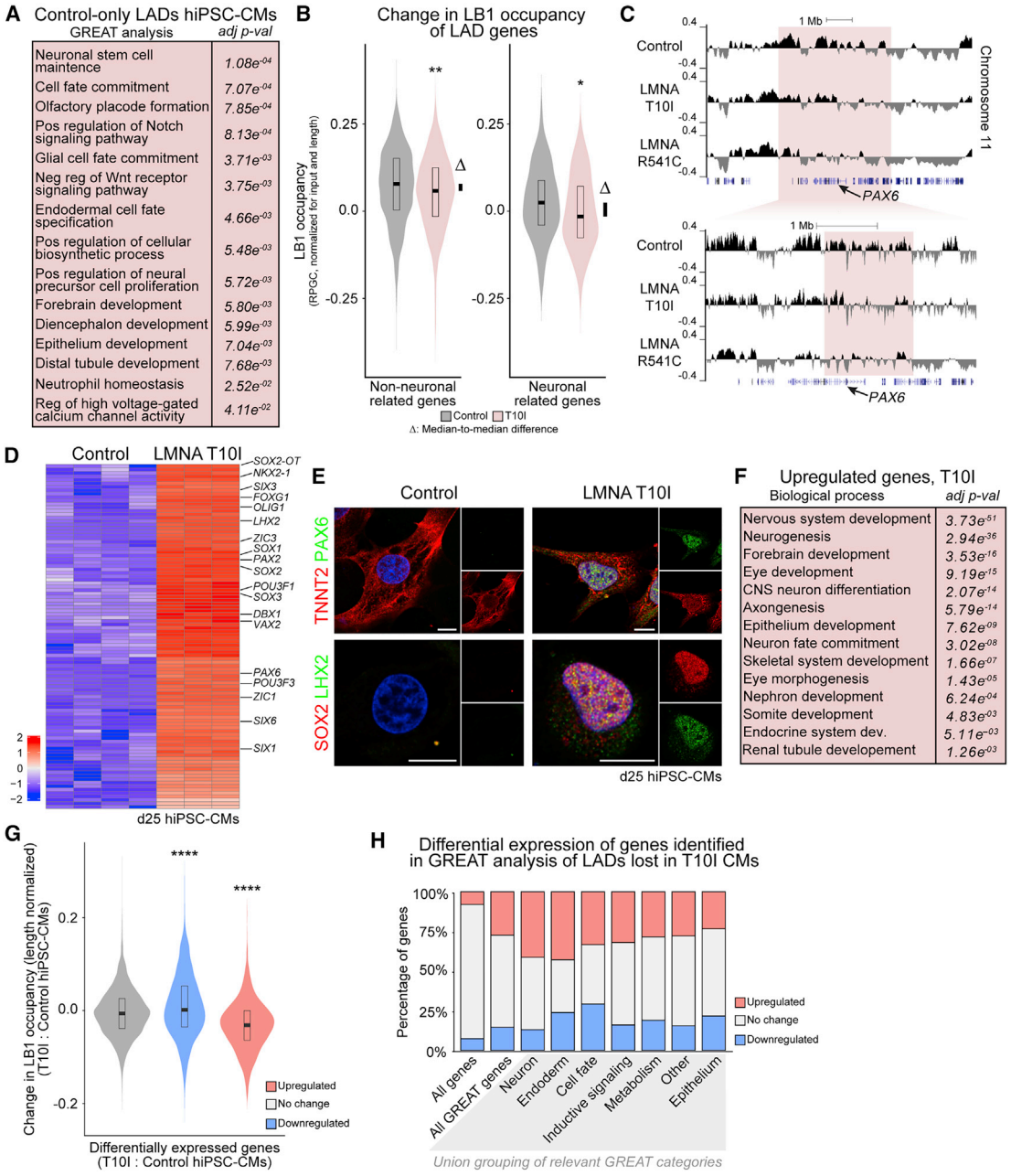

Figure 5. Loss of lamina-bound chromatin in T10I hiPSC-CMs results in non-myocyte gene expression

(A) GREAT analysis of lamina-associated regions found only in the control (defined across biological replicates).

(B) LB1 occupancy of LADs with non-neuronal (left) and neuron-related (right) genes in control (gray) and LMNA T10I (pink) hiPSC-CMs (non-neuronal, Wilcoxon signed rank test with continuity correction; neuronal, paired t test, $p < 0.01$ for non-neuronal, and $p < 0.05$ for neuronal). Δ indicates median-to-median change in LB1 occupancy (neuronal Δ nearly 2× non-neuronal Δ). LAD genes defined by TSS within 50 kb of the EDD-defined LAD.

(C) LB1 ChIP-seq at *PAX6*.

(D) Heatmap of the top 100 upregulated genes by fold change (FDR < 0.05) in T10I d25 hiPSC-CMs compared with the control.

(E) Immunostaining of control and T10I d25 hiPSC-CMs for the indicated antibodies. Scale bars, 10 μm.

(F) Gene Ontology analysis of upregulated genes in T10I hiPSC-CMs compared with the control.

Selected categories are shown for (A) and (F).

(G) Difference in length-normalized LB1 occupancy (T10I minus control) of differentially expressed genes in day 25 T10I hiPSC-CMs (no change, gray; downregulated genes, blue; upregulated genes, red). Differentially expressed genes were defined between T10I and control hiPSC-CMs, day 25 (Kruskal-Wallis rank-sum test, ****$p < 0.0001$ compared with no change).

Boxplots in (B) and (G) indicate median and interquartile range with upper and lower hinges representing 25th and 75th percentiles.

(H) Expression status of genes in each GREAT grouping in T10I compared with control hiPSC-CMs. The leftmost column indicates the overall proportion of up- and downregulated genes.

such as *PAX6*, *SOX2*, and *FOXG1*, showed LB1 depletion in T10I hiPSC-CMs (Figures 5C and S6B). GREAT did not reveal a similar enrichment in T10I-only LADs in hiPSC-CMs (Table S4). Thus, we observed an enrichment of non-myocyte genes in genomic regions uniquely depleted of LB1 occupancy in T10I hiPSC-CMs.

We hypothesized that T10I-mediated disruption of LB1-chromatin interactions affected the expression of genes related to non-myocyte cell types. Overall, expression analysis showed dysregulation of ~15% of genes in T10I compared with control hiPSC-CMs (Figure S6C; Table S2; log2FC $\geq$ |1.5|, false discovery rate [FDR] < 0.05). We observed that the most upregulated genes included multiple factors relevant to non-cardiac myocyte identity, including several related to neuronal biology (Figures 5D and S6D). Quantitative reverse-transcriptase PCR validated the upregulation of various neuronal genes in mutant compared with control hiPSC-CMs (Figure S7A). Immunostaining and immunoblotting confirmed increased protein levels of various non-cardiac genes in T10I hiPSC-CMs, including *PAX6*, *SOX2*, and *LHX2* (Figures 5E, S7B, S7C). Likewise, Gene Ontology analysis of all upregulated T10I hiPSC-CM genes revealed dozens of non-cardiac categories, including nephron development, epithelial biology, and neuronal development (Figure 5F; Table S5). Unsupervised analysis of LAD regions present in control but not R541C hiPSC-CMs also demonstrated neuronal gene enrichment (Figures 5C, S6A, and S6B; Table S4). Parallel to the T10I expression changes, we detected increased expression of myriad genes relevant to non-myocyte identity in R541C hiPSC-CMs compared with control cells (Figures S6C and S6D; Table S2).

To connect these analyses, we determined whether genes losing lamina-chromatin interactions are dysregulated and vice versa. First, genes upregulated in T10I hiPSC-CMs compared with control cells demonstrated a reduction in LB1 occupancy. Conversely, genes downregulated in T10I hiPSC-CMs compared with control cells exhibited an increase in LB1 occupancy (Figure 5G). Reciprocally, we assessed the expression change of genes in the top ~250 control-only or T10I-only lamina-associated regions (e.g., the highest-confidence LB1-enriched regions consistently across the individual replicates). Genes in T10I-only hiPSC-CM lamina-associated regions were preferentially downregulated in T10I hiPSC-CMs (Figure S7D). Conversely, genes located in control-only hiPSC-CM lamina-associated regions were preferentially upregulated in T10I hiPSC-CMs, including multiple genes related to neural identity (Figure S7D). Not all such genes followed this specific expression pattern, suggesting that local transcriptional dysregulation is not sufficient to drive a change across all lamina-chromatin interactions at the sensitivity of the assays employed. A subset of non-LAD genes are affected by *LMNA* mutation, but genes in disrupted LAD regions appear to be dysregulated more often (Figures S6C and S7D). We also combined individual GREAT categories into broad groupings (n = 203 unique genes across 7 groupings) and scored the expression of genes in each grouping as upregulated, downregulated, or unchanged in T10I compared with control hiPSC-CMs. GREAT groupings were enriched for genes that are dysregulated (usually upregulated) in T10I hiPSC-CMs compared with background dysregulation (Figure 5H). These collective analyses indicated that T10I- and R541C-mediated changes in LB1-chromatin organization and in gene expression correlate and lead to impaired silencing of alternative cell type pathways in mutant cells.

Finally, we determined whether analogous changes exist in human cardiac laminopathy. We assessed myocardium expression data from five individuals with DCM with *LMNA* variants (Cheedipudi et al., 2019) or idiopathic DCM (Tan et al., 2020), compared them with their linked non-failing control myocardium, and identified upregulated genes in *LMNA* or idiopathy DCM. Approximately 1,880 genes were upregulated in *LMNA* mutant but not idiopathic DCM myocardium (Figure 6A). Strikingly, Gene Ontology analysis of the ~1,880 genes revealed an enrichment for non-cardiac cellular identity (Figure 6A; Table S5), specifically neurobiology. We created a *LMNA* non-myocyte identity signature gene set by combining ontology category genes (Figure 6A). We assessed expression (no change, upregulated, or downregulated) in T10I hiPSC-CMs of genes in the *LMNA*-specific myocardium and the *LMNA* non-myocyte identity signature gene sets. Gene sets were filtered to include only genes represented in hiPSC-CM expression data. Approximately 12% of genes identified in the *LMNA* mutant myocardium gene set were also differentially expressed in T10I hiPSC-CMs using stringent criteria (n = 1,715 genes; log2 FC $\geq$ |1.5|, adjusted $p < 0.05$), and ~31% genes in the *LMNA* myocardium non-myocyte identity signature set were differentially expressed in T10I hiPSC-CMs (n = 727 genes; Figure 6B). Moreover, LB1 occupancy of the *LMNA* myocardium non-myocyte signature gene set was decreased significantly in T10I hiPSC-CMs compared with control cells (Figure 6C). Stratification by expression in T10I hiPSC-CMs demonstrated an inverse relationship to LB1 occupancy, with the largest effect being LB1 occupancy loss in upregulated genes (Figure 6C, plots in boxes). This trend was also observed when we performed a similar analysis using the total *LMNA* mutant myocardium gene set (Figure S7E). These data indicate that the aberrant expression of non-cardiac myocyte lineage genes, as revealed in T10I- and R541C hiPSC-CM models, may reflect a parallel phenotype in human cardiac laminopathies.

DISCUSSION

Peripheral chromatin organization provides a critical layer of gene regulation, but physiological examples illustrating functional relevance have been elusive, perhaps because of mechanistic heterogeneity or studies in cell types unable to manifest functional change. We demonstrate that an amino acid substitution in one allele of *LMNA* (T10I or R541C) in hiPSC-CMs is sufficient to disrupt genome-lamina interactions during CM development, altering gene expression and cellular physiology. Our results strongly support a model in which T10I, R541C, and likely other pathogenic *LMNA* variants result in targeted aberrations in peripheral chromatin regions in specific cell types and are linked to aberrant expression of alternative fate genes (Figure 7).

Lamina-chromatin interactions protect cellular identity

Alternative lineage genes gain LAD residence during murine cardiac differentiation (Poleshko et al., 2017), and perinuclear chromatin sequestration stabilizes fate commitment in worms (Gonzalez-Sandoval et al., 2015). Our study extends these observations in two ways. First, three different hiPSC-derived cell

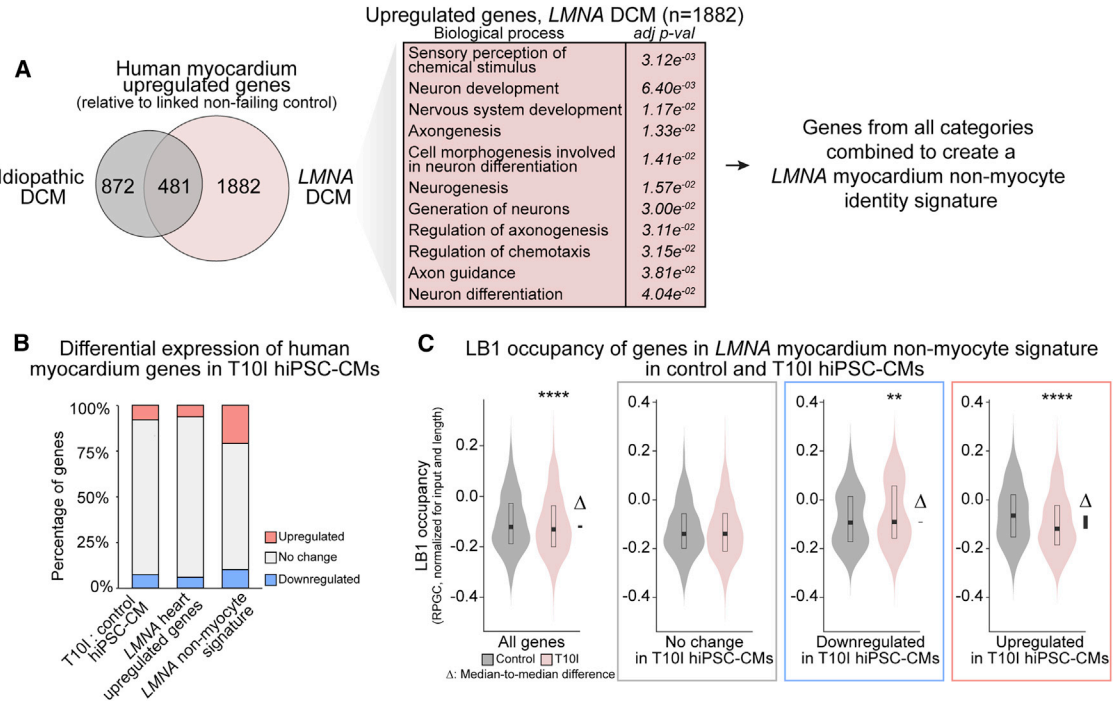

Figure 6. The human *LMNA* DCM myocardium signature shows LB1 loss in hiPSC-CMs

(A) Overlap of upregulated genes in idiopathic DCM compared with *LMNA* DCM from published datasets (each compared with the respective/linked non-failing controls; *LMNA* DCM:non-failing control [Cheedipudi et al., 2019], idiopathic DCM:non-failing control [Tan et al., 2020]). 1,882 genes are uniquely upregulated in *LMNA*-linked disease; Gene Ontology analysis shows enrichment for neuronal genes (adj. p values are shown in the right column; selected categories are shown). Genes from categories were combined to define a *LMNA* myocardium non-myocyte gene signature; n = 727 genes after expression filtering.

(B) Differential expression of human myocardium genes in T10I hiPSC-CMs (left column, T10I compared with control hiPSC-CMs; center column, *LMNA* myocardium upregulated genes; right column, *LMNA* myocardium non-myocyte signature; for the center and right columns, only genes represented in the hiPSC-CM RNA-seq dataset were included; 3×3 $\chi^2 = 185.22$ with 4 degrees of freedom, $p < 0.0001$).

(C) LB1 occupancy in control and T10I hiPSC-CMs (day 25) of genes in *LMNA* myocardium non-myocyte signature. Δ indicates median-to-median change in LB1 occupancy. Adjacent boxes show the LB1 occupancy in control and T10I hiPSC-CMs of the subset of genes that were not changed (gray box), downregulated (blue box), and upregulated (red box). Wilcoxon signed-rank test with continuity correction; ****$p < 0.0001$, **$p < 0.01$; the boxplot indicates median and inter-quartile range with upper and lower hinges representing 25th and 75th percentiles.

types demonstrate lineage-specific peripheral organization. Cells along one differentiation trajectory show minimal LAD changes as the lineage restricts (Peric-Hupkes et al., 2010). Our data suggest that cells from more distant lineages may have fewer "shared" LADs. A more robust atlas of LAD maps across germ layers and cell types will better assess the extent of "invariant" or "constitutive" LADs (Keough et al., 2020). Second, we showed that two pathogenic *LMNA* variants preferentially affected peripheral chromatin organization in hiPSC-CMs compared with hiPSC-heps and hiPSC-adips. A subset of T10I hiPSC-CMs displayed abnormal morphology prior to visible contraction. T10I also resulted in a mild effect in hiPSC-adip morphology—minor relative to hiPSC-CM mutants—and could relate to the patient's lipid abnormalities. The variants resulted in loss of LB1 occupancy and increased expression of non-myocyte genes during cardiac differentiation despite equivalent cardiac specification in controls and mutants. Thus, our data suggest that *LMNA* variants, in part, abrogate silencing of non-myocyte genes in hiPSC-CMs.

Lamin dimers are arranged in a head-to-tail conformation; dimers assemble into larger filaments and arrays implicated in the maintenance of nuclear shape (Dechat et al., 2010). It is possible that T10I (head domain) and R541C (tail domain) affect the dimer and result in a defective filament, leading to abnormal nuclear morphology and organization in mutant hiPSC-CMs. Compartment changes and misexpression of neuronal genes have been observed in *LMNA*-haploinsufficient hiPSC-CMs (Bertero et al., 2019). In addition, overexpression of a *LMNA* variant in immortalized cells is also linked to misexpression of lineage genes (Perovanovic et al., 2016), a lipodystrophic *LMNA* variant affects endothelial differentiation (Briand et al., 2018), and LADs are affected in hiPSC-CMs with a truncating *LMNA* variant (Lee et al., 2019). This suggests that there could be overlapping molecular consequences of missense and frameshift *LMNA* mutations. In addition, although LAMIN B1 is exclusively at the lamina, a pool of LAMIN A/C filaments is found in the nuclear interior (Gesson et al., 2016; Ikegami et al., 2020). Super-high-resolution imaging reveals lamin microdomains (Shimi et al., 2015; Xie et al., 2016), but given the high degree of LAMIN A/B1 co-occupancy (Meuleman et al., 2013), it is possible that domains are not patterned uniformly. It will be interesting to determine how pathologic variants affect LAMIN A/C in a model engineered to distinguish mutant versus wild-type LAMIN A/C.

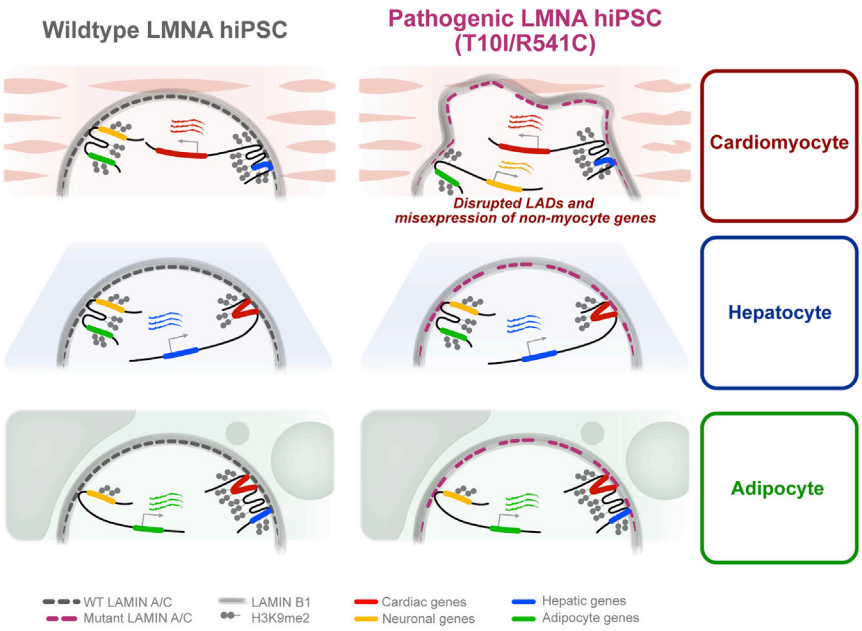

Figure 7. Model

Cells have tissue-specific LAD maps. LADs with genes and lower LB1 contact frequency specifically lose LB1 association in mutant hiPSC-CMs. Genes relevant to alternative lineages lose LB1 contact and are expressed in mutant hiPSC-CMs. Mutant hiPSC-hep or -adip LADs are minimally different from control hiPSC-heps or -adips.

LMNA T10I and R541C preferentially affect a specific subset of peripheral chromatin in CMs

This work unveiled a critical aspect of general LAD organization: a subset of gene-rich and LB1-poor LADs are distinguishable from gene-poor and LB1-rich LADs in location and vulnerability to pathogenic *LMNA* variants. LADs vary with respect to DNA sequence enrichment, histone modification, and gene expression (Guelen et al., 2008; Harr et al., 2015; Leemans et al., 2019; Meuleman et al., 2013; Wen et al., 2009; Zullo et al., 2012); however, the functional relevance of this heterogeneity is unknown. Our data demonstrate that *LMNA* variants specifically target LADs with definable molecular features, raising the possibility that multiple mechanisms may establish or maintain different regions of peripheral chromatin. Consistently, depletion of multiple lamin filaments results in LADs with low contact frequency repositioning to the nuclear interior, whereas LADs with strong contact with the lamina de-condense but do not reposition (Zheng et al., 2018).

Our data suggest that a key mechanism to maintain nuclear architecture involves proper organization of H3K9me2-bound chromatin at the lamina. We observed ''uncoupling'' of H3K9me2 and LB1 co-occupancy in T10I and R541C hiPSC-CMs but not in hiPSC-heps or hiPSC-adips. One mechanism to maintain peripheral organization may involve protein complexes tethering chromatin. Cec4 is one such tether of H3K9-methylated chromatin in *C. elegans* (Gonzalez-Sandoval et al., 2015), but a mammalian ortholog is undefined. Proteomics-based studies show tissue-specific expression of nuclear envelope proteins (Korfali et al., 2012), and tissue-specific protein nuclear envelope proteins regulate LADs during skeletal myoblast differentiation (Robson et al., 2016). Identification of such proteins in mammalian cells will help elucidate how cell-type-specific peripheral chromatin is organized. Identification of H3K9 methyl readers may reveal whether *LMNA* variants affect H3K9me2 reader localization. Consistently, manipulation of lysine 9 on histone H3 resulted in loss of peripheral chromatin organization (Poleshko et al., 2019), underscoring the utility of T10I, R541C, and other *LMNA* variant models in understanding how specific regions of the genome in specific cell types are located to the nuclear periphery.

Additional mechanisms likely also govern specific peripheral organization. For example, long non-coding RNA transcription has been hypothesized to direct nuclear architecture (Melé and Rinn, 2016), *Xist* mediates positioning of the inactive X chromosome at the lamina (Chen et al., 2016), and *ThymoD* modulates positioning of a critical enhancer (Isoda et al., 2017). The flexible structure of RNA provides an attractive method to organize dynamic peripheral chromatin. Another mechanism may involve signal transduction cascades coalescing on epigenetic factors that regulate peripheral chromatin. For example, casein kinase II-dependent BRD4 phosphorylation regulates its chromatin binding (Wu et al., 2013), and similar examples have emerged for HDAC2, TIP60, and others. Our data reveal a specific class of peripheral chromatin that is susceptible to *LMNA* variant-mediated changes, and it will be exciting to discover the various mechanisms that regulate organization of each of these classes in future work.

Limitations of study

Our study utilizes hiPSC-derived cell types, which are relatively immature and do not reflect aging, circulating factors, and tissue cross-talk affect physiology. We cannot exclude that physiological factors and/or further maturation may reveal additional LAD changes. A second limitation is inherent in population-based genomics. Aspects of genome organization demonstrate cell-to-cell variability (Bintu et al., 2018; Finn et al., 2019; Kind et al., 2015); however, technological limitations are a barrier to many genome-wide assessments in single cells. Advances in technology, including single-cell ChIP methods and improved higher-throughput imaging approaches, will help overcome these barriers. A similar limitation arises from data. The disease and control RNA-seq datasets are from human myocardium, and we cannot rule out a change in cellular composition, particularly in *LMNA* versus idiopathic DCM or the effect of heterogenous gene expression. Generating single-cell gene expression datasets for the normal and diseased human heart will help address this limitation, but datasets from dozens of samples will likely be required to overcome individual variability. Finally, our hiPSC lines demonstrate the sufficiency of two particular *LMNA* variants to affect genome organization in hiPSC-CMs versus

hiPSC-adips or -heps. Manifestation of individual phenotypes likely requires additional factors, such as enhancer and suppressor variants. It will be revealing to extend the current studies with additional hiPSC lines to determine how phenotypes elicited by these and other variants are affected by additional modifier loci.

Our data argue against cardiac laminopathy phenotypes resulting from widescale or stochastic nuclear organization changes. We demonstrate the importance of studying laminopathies in the appropriate cellular context to identify how lamina-bound chromatin with a unique molecular signature is affected in specific cell types.

STAR★METHODS

Detailed methods are provided in the online version of this paper and include the following:

- KEY RESOURCES TABLE
- RESOURCE AVAILABILITY
  - Lead contact
  - Materials availability
  - Data and code availability
- EXPERIMENTAL MODEL AND SUBJECT DETAILS
  - hiPSC Line Culturing
  - Human Myocardial Studies
- METHOD DETAILS
  - hiPSC Line Creation and Validation
  - hiPSC-Cardiomyocyte Differentiation
  - Flow Cytometry
  - Calcium Measurements
  - Atomic Force Microscopy
  - Fabrication of 3D Micropatterned Cardiac Cultures
  - Micropatterned Cardiac Culture Contractility Analyses
  - Human Myocardial Gene Expression Analysis
  - hiPSC-Hepatocyte Differentiation
  - hiPSC-Adipocyte Differentiation
  - Protein Isolation and Immunoblot Analysis
  - Immunofluorescence
  - ChIP and ChIP-seq Library Preparation
  - RNA Isolation and RNA-seq Library Preparation
  - ChIP-seq Analysis
  - RNA-seq Analysis
- QUANTIFICATION AND STATISTICAL ANALYSIS

SUPPLEMENTAL INFORMATION

Supplemental Information can be found online at https://doi.org/10.1016/j.stem.2020.12.016.

ACKNOWLEDGMENTS

We thank C.L. Smith and J.A. Epstein for critical discussions, S.R. Jain and N.A. Islam for early cell culture work, and Ana Silva (ana@anasilvaillustrations.com) for expert assistance with graphical design. This work was supported by the Burroughs Wellcome Career Award for Medical Scientists; a Gilead Research Scholars Award; the Pennsylvania Department of Health; the American Heart Association/Allen Initiative; NIH DP2 HL147123 (to R.J.), R35 HL145203 (to K.M.), R01 HL149891 (to B.L.P.), R01 HL130006 (to J.C.W.), R01HL141371 (to J.C.W.), K08HL140129 and Ayla Gunner Prushansky Research Fund (to D.B.F.), F31 HL147416 (to R.L.-S.), NSF15-48571 (to B.L.P, J.G.H., R.L.-S., and R.J.), and R01 GM137425; the Penn Institute for Regenerative Medicine (to W.Y.); and the Winkelman Family Fund for Cardiac Innovation (to A.T.O. and K.M.).

AUTHOR CONTRIBUTIONS

P.P.S., W.L., K.M., and R.J. conceived the project and wrote the manuscript. P.P.S., W.L., A.P., D.A., D.J.R., J.G.H., M.A.C., B.L.P., D.T., N.S., J.C.W., R.L.-S., Q.W., L.J.S., K.B., W.Y., and D.B.F. contributed to wet laboratory experiments. J.H.R., M.P.M., and T.P.C. contributed to bioinformatic and genetic analyses. A.T.O. and K.B.M. enrolled participants in the study protocol. K.M. and R.J. supervised the project. All authors read and approved the manuscript.

DECLARATION OF INTERESTS

K.M. is an advisor to and holds equity in Variant Bio and Verve Therapeutics.

Received: July 28, 2020
Revised: October 13, 2020
Accepted: December 18, 2020
Published: February 1, 2021

REFERENCES

Benjamini, Y., and Hochberg, Y. (1995). Controlling the False Discovery Rate: A Practical and Powerful Approach to Multiple Testing. J. R. Stat. Soc. B Methodol. *57*, 289–300.

Bertero, A., Fields, P.A., Smith, A.S.T., Leonard, A., Beussman, K., Sniadecki, N.J., Kim, D.-H., Tse, H.-F., Pabon, L., Shendure, J., et al. (2019). Chromatin compartment dynamics in a haploinsufficient model of cardiac laminopathy. J. Cell Biol. *218*, 2919–2944.

Bintu, B., Mateo, L.J., Su, J.H., Sinnott-Armstrong, N.A., Parker, M., Kinrot, S., Yamaya, K., Boettiger, A.N., and Zhuang, X. (2018). Super-resolution chromatin tracing reveals domains and cooperative interactions in single cells. Science *362*, eaau1783.

Blighe, K., and Lun, A. (2019). PCAtools: everything Principal Components Analysis. https://github.com/kevinblighe/PCAtools.

Bolger, A.M., Lohse, M., and Usadel, B. (2014). Trimmomatic: A flexible trimmer for Illumina Sequence Data. Bioinformatics *30*, 2114–2120, https://doi.org/10.1093/bioinformatics/btu170.

Brady, G.F., Kwan, R., Bragazzi Cunha, J., Elenbaas, J.S., and Omary, M.B. (2018). Lamins and Lamin-Associated Proteins in Gastrointestinal Health and Disease. Gastroenterology *154*, 1602–1619.e1.

Briand, N., and Collas, P. (2020). Lamina-associated domains: peripheral matters and internal affairs. Genome Biol. *21*, 85.

Briand, N., Guénantin, A.C., Jeziorowska, D., Shah, A., Mantecon, M., Capel, E., Garcia, M., Oldenburg, A., Paulsen, J., Hulot, J.S., et al. (2018). The lipodystrophic hotspot lamin A p.R482W mutation deregulates the mesodermal inducer T/Brachyury and early vascular differentiation gene networks. Hum. Mol. Genet. *27*, 1447–1459.

Burke, B., and Stewart, C.L. (2006). The laminopathies: the functional architecture of the nucleus and its contribution to disease. Annu. Rev. Genomics Hum. Genet. *7*, 369–405.

Cai, J., DeLaForest, A., Fisher, J., Urick, A., Wagner, T., Twaroski, K., Cayo, M., Nagaoka, M., and Duncan, S.A. (2008). Protocol for directed differentiation of human pluripotent stem cells toward a hepatocyte fate. StemBook. https://doi.org/10.3824/stembook.1.52.1.

Cheedipudi, S.M., Matkovich, S.J., Coarfa, C., Hu, X., Robertson, M.J., Sweet, M., Taylor, M., Mestroni, L., Cleveland, J., Willerson, J.T., et al. (2019). Genomic Reorganization of Lamin-Associated Domains in Cardiac Myocytes Is Associated With Differential Gene Expression and DNA Methylation in Human Dilated Cardiomyopathy. Circ. Res. *124*, 1198–1213.

Chen, C.K., Blanco, M., Jackson, C., Aznauryan, E., Ollikainen, N., Surka, C., Chow, A., Cerase, A., McDonel, P., and Guttman, M. (2016). Xist recruits the X chromosome to the nuclear lamina to enable chromosome-wide silencing. Science *354*, 468–472.

Chen, C.Y., Caporizzo, M.A., Bedi, K., Vite, A., Bogush, A.I., Robison, P., Heffler, J.G., Salomon, A.K., Kelly, N.A., Babu, A., et al. (2018). Suppression of detyrosinated microtubules improves cardiomyocyte function in human heart failure. Nat. Med. *24*, 1225–1233.

Cho, S., Vashisth, M., Abbas, A., Majkut, S., Vogel, K., Xia, Y., Ivanovska, I.L., Irianto, J., Tewari, M., Zhu, K., et al. (2019). Mechanosensing by the Lamina Protects against Nuclear Rupture, DNA Damage, and Cell-Cycle Arrest. Dev. Cell *49*, 920–935.e5.

de Leeuw, R., Gruenbaum, Y., and Medalia, O. (2018). Nuclear Lamins: Thin Filaments with Major Functions. Trends Cell Biol. *28*, 34–45.

Dechat, T., Adam, S.A., Taimen, P., Shimi, T., and Goldman, R.D. (2010). Nuclear lamins. Cold Spring Harb. Perspect. Biol. *2*, a000547.

Dipla, K., Mattiello, J.A., Jeevanandam, V., Houser, S.R., and Margulies, K.B. (1998). Myocyte recovery after mechanical circulatory support in humans with end-stage heart failure. Circulation *97*, 2316–2322.

Dobin, A., Davis, C.A., Schlesinger, F., Drenkow, J., Zaleski, C., Jha, S., Batut, P., Chaisson, M., and Gingeras, T.R. (2013). STAR: ultrafast universal RNA-seq aligner. Bioinformatics *29*, 15–21.

Finn, E.H., Pegoraro, G., Brandao, H.B., Valton, A.L., Oomen, M.E., Dekker, J., Mirny, L., and Misteli, T. (2019). Extensive Heterogeneity and Intrinsic Variation in Spatial Genome Organization. Cell *176*, 1502–1515.e10.

Gesson, K., Rescheneder, P., Skoruppa, M.P., von Haeseler, A., Dechat, T., and Foisner, R. (2016). A-type lamins bind both hetero- and euchromatin, the latter being regulated by lamina-associated polypeptide 2 alpha. Genome Res. *26*, 462–473.

Gonzalez-Sandoval, A., Towbin, B.D., Kalck, V., Cabianca, D.S., Gaidatzis, D., Hauer, M.H., Geng, L., Wang, L., Yang, T., Wang, X., et al. (2015). Perinuclear Anchoring of H3K9-Methylated Chromatin Stabilizes Induced Cell Fate in C. elegans Embryos. Cell *163*, 1333–1347.

Gu, Z., Eils, R., and Schlesner, M. (2016). Complex heatmaps reveal patterns and correlations in multidimensional genomic data. Bioinformatics *32*, 2847–2849.

Guelen, L., Pagie, L., Brasset, E., Meuleman, W., Faza, M.B., Talhout, W., Eussen, B.H., de Klein, A., Wessels, L., de Laat, W., and van Steensel, B. (2008). Domain organization of human chromosomes revealed by mapping of nuclear lamina interactions. Nature *453*, 948–951.

Hale, C.M., Shrestha, A.L., Khatau, S.B., Stewart-Hutchinson, P.J., Hernandez, L., Stewart, C.L., Hodzic, D., and Wirtz, D. (2008). Dysfunctional connections between the nucleus and the actin and microtubule networks in laminopathic models. Biophys. J. *95*, 5462–5475.

Harr, J.C., Luperchio, T.R., Wong, X., Cohen, E., Wheelan, S.J., and Reddy, K.L. (2015). Directed targeting of chromatin to the nuclear lamina is mediated by chromatin state and A-type lamins. J. Cell Biol. *208*, 33–52.

Harr, J.C., Schmid, C.D., Muñoz-Jiménez, C., Romero-Bueno, R., Kalck, V., Gonzalez-Sandoval, A., Hauer, M.H., Padeken, J., Askjaer, P., Mattout, A., and Gasser, S.M. (2020). Loss of an H3K9me anchor rescues laminopathy-linked changes in nuclear organization and muscle function in an Emery-Dreifuss muscular dystrophy model. Genes Dev. *34*, 560–579.

Houben, F., Ramaekers, F.C., Snoeckx, L.H., and Broers, J.L. (2007). Role of nuclear lamina-cytoskeleton interactions in the maintenance of cellular strength. Biochim. Biophys. Acta *1773*, 675–686.

Huebsch, N., Loskill, P., Mandegar, M.A., Marks, N.C., Sheehan, A.S., Ma, Z., Mathur, A., Nguyen, T.N., Yoo, J.C., Judge, L.M., et al. (2015). Automated Video-Based Analysis of Contractility and Calcium Flux in Human-Induced Pluripotent Stem Cell-Derived Cardiomyocytes Cultured over Different Spatial Scales. Tissue Eng. Part C Methods *21*, 467–479.

Hussain, I., Patni, N., Ueda, M., Sorkina, E., Valerio, C.M., Cochran, E., Brown, R.J., Peeden, J., Tikhonovich, Y., Tiulpakov, A., et al. (2018). A Novel Generalized Lipodystrophy-Associated Progeroid Syndrome Due to Recurrent Heterozygous LMNA p.T10I Mutation. J. Clin. Endocrinol. Metab. *103*, 1005–1014.

Hutchison, C.J. (2002). Lamins: building blocks or regulators of gene expression? Nat. Rev. Mol. Cell Biol. *3*, 848–858.

Ikegami, K., Secchia, S., Almakki, O., Lieb, J.D., and Moskowitz, I.P. (2020). Phosphorylated Lamin A/C in the Nuclear Interior Binds Active Enhancers Associated with Abnormal Transcription in Progeria. Dev. Cell *52*, 699–713.e11.

Isoda, T., Moore, A.J., He, Z., Chandra, V., Aida, M., Denholtz, M., Piet van Hamburg, J., Fisch, K.M., Chang, A.N., Fahl, S.P., et al. (2017). Non-coding Transcription Instructs Chromatin Folding and Compartmentalization to Dictate Enhancer-Promoter Communication and T Cell Fate. Cell *171*, 103–119.e18.

Keough, K.C., Shah, P.P., Wickramasinghe, N.M., Dundes, C.E., Chen, A., Salomon, R.E.A., Whalen, S., Loh, K.M., Dubois, N., Pollard, K.S., et al. (2020). An atlas of lamina-associated chromatin across thirteen human cell types reveals cell-type-specific and multiple subtypes of peripheral heterochromatin. bioRxiv. https://doi.org/10.1101/2020.07.23.218768.

Khatau, S.B., Hale, C.M., Stewart-Hutchinson, P.J., Patel, M.S., Stewart, C.L., Searson, P.C., Hodzic, D., and Wirtz, D. (2009). A perinuclear actin cap regulates nuclear shape. Proc. Natl. Acad. Sci. USA *106*, 19017–19022.

Kind, J., Pagie, L., Ortabozkoyun, H., Boyle, S., de Vries, S.S., Janssen, H., Amendola, M., Nolen, L.D., Bickmore, W.A., and van Steensel, B. (2013). Single-cell dynamics of genome-nuclear lamina interactions. Cell *153*, 178–192.

Kind, J., Pagie, L., de Vries, S.S., Nahidiazar, L., Dey, S.S., Bienko, M., Zhan, Y., Lajoie, B., de Graaf, C.A., Amendola, M., et al. (2015). Genome-wide maps of nuclear lamina interactions in single human cells. Cell *163*, 134–147.

Korfali, N., Wilkie, G.S., Swanson, S.K., Srsen, V., de Las Heras, J., Batrakou, D.G., Malik, P., Zuleger, N., Kerr, A.R., Florens, L., and Schirmer, E.C. (2012). The nuclear envelope proteome differs notably between tissues. Nucleus *3*, 552–564.

Lammerding, J., Schulze, P.C., Takahashi, T., Kozlov, S., Sullivan, T., Kamm, R.D., Stewart, C.L., and Lee, R.T. (2004). Lamin A/C deficiency causes defective nuclear mechanics and mechanotransduction. J. Clin. Invest. *113*, 370–378.

Lang, R.M., Bierig, M., Devereux, R.B., Flachskampf, F.A., Foster, E., Pellikka, P.A., Picard, M.H., Roman, M.J., Seward, J., Shanewise, J., et al.; American Society of Echocardiography's Nomenclature and Standards Committee; Task Force on Chamber Quantification; American College of Cardiology Echocardiography Committee; American Heart Association; European Association of Echocardiography, European Society of Cardiology (2006). Recommendations for chamber quantification. Eur. J. Echocardiogr. *7*, 79–108.

Lee, J.S., Hale, C.M., Panorchan, P., Khatau, S.B., George, J.P., Tseng, Y., Stewart, C.L., Hodzic, D., and Wirtz, D. (2007). Nuclear lamin A/C deficiency induces defects in cell mechanics, polarization, and migration. Biophys. J. *93*, 2542–2552.

Lee, J., Termglinchan, V., Diecke, S., Itzhaki, I., Lam, C.K., Garg, P., Lau, E., Greenhaw, M., Seeger, T., Wu, H., et al. (2019). Activation of PDGF pathway links LMNA mutation to dilated cardiomyopathy. Nature *572*, 335–340.

Leemans, C., van der Zwalm, M.C.H., Brueckner, L., Comoglio, F., van Schaik, T., Pagie, L., van Arensbergen, J., and van Steensel, B. (2019). Promoter-Intrinsic and Local Chromatin Features Determine Gene Repression in LADs. Cell *177*, 852–864.e14.

Li, H., and Durbin, R. (2009). Fast and accurate short read alignment with Burrows-Wheeler Transform. Bioinformatics *25*, 1754–1760, https://doi.org/10.1093/bioinformatics/btp324.

Li, H., Handsaker, B., Wysoker, A., Fennell, T., Ruan, J., Homer, N., Marth, G., Abecasis, G., and Durbin, R.; 1000 Genome Project Data Processing Subgroup (2009). The Sequence Alignment/Map format and SAMtools. Bioinformatics *25*, 2078–2079, https://doi.org/10.1093/bioinformatics/btp352.

Lian, X., Zhang, J., Azarin, S.M., Zhu, K., Hazeltine, L.B., Bao, X., Hsiao, C., Kamp, T.J., and Palecek, S.P. (2013). Directed cardiomyocyte differentiation from human pluripotent stem cells by modulating Wnt/β-catenin signaling under fully defined conditions. Nat. Protoc. *8*, 162–175.

Liao, Y., Smyth, G.K., and Shi, W. (2019). The R package Rsubread is easier, faster, cheaper and better for alignment and quantification of RNA sequencing reads. Nucleic Acids Res. *47*, e47.

Lund, E., Oldenburg, A.R., and Collas, P. (2014). Enriched domain detector: a program for detection of wide genomic enrichment domains robust against local variations. Nucleic Acids Res. *42*, e92.

McCarthy, D.J., Chen, Y., and Smyth, G.K. (2012). Differential expression analysis of multifactor RNA-Seq experiments with respect to biological variation. Nucleic Acids Res. *40*, 4288–4297.

McKee, C.T., Raghunathan, V.K., Nealey, P.F., Russell, P., and Murphy, C.J. (2011). Topographic modulation of the orientation and shape of cell nuclei and their influence on the measured elastic modulus of epithelial cells. Biophys. J. *101*, 2139–2146.

McLean, C.Y., Bristor, D., Hiller, M., Clarke, S.L., Schaar, B.T., Lowe, C.B., Wenger, A.M., and Bejerano, G. (2010). GREAT improves functional interpretation of cis-regulatory regions. Nat. Biotechnol. *28*, 495–501.

Meister, P., Towbin, B.D., Pike, B.L., Ponti, A., and Gasser, S.M. (2010). The spatial dynamics of tissue-specific promoters during C. elegans development. Genes Dev. *24*, 766–782.

Melé, M., and Rinn, J.L. (2016). "Cat's Cradling" the 3D Genome by the Act of LncRNA Transcription. Mol. Cell *62*, 657–664.

Merrick, D., Sakers, A., Irgebay, Z., Okada, C., Calvert, C., Morley, M.P., Percec, I., and Seale, P. (2019). Identification of a mesenchymal progenitor cell hierarchy in adipose tissue. Science *364*, eaav2501, https://doi.org/10.1126/science.aav2501.

Meuleman, W., Peric-Hupkes, D., Kind, J., Beaudry, J.B., Pagie, L., Kellis, M., Reinders, M., Wessels, L., and van Steensel, B. (2013). Constitutive nuclear lamina-genome interactions are highly conserved and associated with A/T-rich sequence. Genome Res. *23*, 270–280.

Mewborn, S.K., Puckelwartz, M.J., Abuisneineh, F., Fahrenbach, J.P., Zhang, Y., MacLeod, H., Dellefave, L., Pytel, P., Selig, S., Labno, C.M., et al. (2010). Altered chromosomal positioning, compaction, and gene expression with a lamin A/C gene mutation. PLoS ONE *5*, e14342.

Paulsen, J., Liyakat Ali, T.M., Nekrasov, M., Delbarre, E., Baudement, M.O., Kurscheid, S., Tremethick, D., and Collas, P. (2019). Long-range interactions between topologically associating domains shape the four-dimensional genome during differentiation. Nat. Genet. *51*, 835–843.

Peric-Hupkes, D., and van Steensel, B. (2010). Role of the nuclear lamina in genome organization and gene expression. Cold Spring Harb. Symp. Quant. Biol. *75*, 517–524.

Peric-Hupkes, D., Meuleman, W., Pagie, L., Bruggeman, S.W., Solovei, I., Brugman, W., Gräf, S., Flicek, P., Kerkhoven, R.M., van Lohuizen, M., et al. (2010). Molecular maps of the reorganization of genome-nuclear lamina interactions during differentiation. Mol. Cell *38*, 603–613.

Perovanovic, J., Dell'Orso, S., Gnochi, V.F., Jaiswal, J.K., Sartorelli, V., Vigouroux, C., Mamchaoui, K., Mouly, V., Bonne, G., and Hoffman, E.P. (2016). Laminopathies disrupt epigenomic developmental programs and cell fate. Sci. Transl. Med. *8*, 335ra58.

Poleshko, A., Shah, P.P., Gupta, M., Babu, A., Morley, M.P., Manderfield, L.J., Ifkovits, J.L., Calderon, D., Aghajanian, H., Sierra-Pagán, J.E., et al. (2017). Genome-Nuclear Lamina Interactions Regulate Cardiac Stem Cell Lineage Restriction. Cell *171*, 573–587.e14.

Poleshko, A., Smith, C.L., Nguyen, S.C., Sivaramakrishnan, P., Wong, K.G., Murray, J.I., Lakadamyali, M., Joyce, E.F., Jain, R., and Epstein, J.A. (2019). H3K9me2 orchestrates inheritance of spatial positioning of peripheral heterochromatin through mitosis. eLife *8*, e49278.

Quinlan, A.R., and Hall, I.M. (2010). BEDTools: a flexible suite of utilities for comparing genomic features. Bioinformatics *26*, 841–842. Epub 2010 Jan 28. https://doi.org/10.1093/bioinformatics/btq033.

Ramírez, F., Ryan, D.P., Grüning, B., Bhardwaj, V., Kilpert, F., Richter, A.S., Heyne, S., Dündar, F., and Manke, T. (2016). deepTools2: a next generation web server for deep-sequencing data analysis. Nucleic Acids Res. *44*, W160–W165, https://doi.org/10.1093/nar/gkw257.

Rankin, J., and Ellard, S. (2006). The laminopathies: a clinical review. Clin. Genet. *70*, 261–274.

Raudvere, U., Kolberg, L., Kuzmin, I., Arak, T., Adler, P., Peterson, H., and Vilo, J. (2019). g:Profiler: a web server for functional enrichment analysis and conversions of gene lists (2019 update). Nucleic Acids Res. *47* (W1), W191–W198.

R Core Team (2012). R: A Language and Environment for Statistical Computing (Vienna, Austria: R Foundation for Statistical Computing). http://www.R-project.org.

Ritchie, M.E., Phipson, B., Wu, D., Hu, Y., Law, C.W., Shi, W., and Smyth, G.K. (2015). limma powers differential expression analyses for RNA-sequencing and microarray studies. Nucleic Acids Res. *43*, e47.

Robinson, M.D., McCarthy, D.J., and Smyth, G.K. (2010). edgeR: a Bioconductor package for differential expression analysis of digital gene expression data. Bioinformatics *26*, 139–140.

Robson, M.I., de Las Heras, J.I., Czapiewski, R., Lê Thành, P., Booth, D.G., Kelly, D.A., Webb, S., Kerr, A.R.W., and Schirmer, E.C. (2016). Tissue-Specific Gene Repositioning by Muscle Nuclear Membrane Proteins Enhances Repression of Critical Developmental Genes during Myogenesis. Mol. Cell *62*, 834–847.

Ross-Innes, C.S., Stark, R., Teschendorff, A.E., Holmes, K.A., Ali, H.R., Dunning, M.J., Brown, G.D., Gojis, O., Ellis, I.O., Green, A.R., et al. (2012). Differential oestrogen receptor binding is associated with clinical outcome in breast cancer. Nature *481*, 389–393.

See, K., Lan, Y., Rhoades, J., Jain, R., Smith, C.L., and Epstein, J.A. (2019). Lineage-specific reorganization of nuclear peripheral heterochromatin and H3K9me2 domains. Development *146*, dev174078.

Shimi, T., Kittisopikul, M., Tran, J., Goldman, A.E., Adam, S.A., Zheng, Y., Jaqaman, K., and Goldman, R.D. (2015). Structural organization of nuclear lamins A, C, B1, and B2 revealed by superresolution microscopy. Mol. Biol. Cell *26*, 4075–4086.

Stark, R., and Brown, G. (2011). DiffBind: differential binding analysis of ChIP-Seq peak data. https://bioconductor.org/packages/release/bioc/vignettes/DiffBind/inst/doc/DiffBind.pdf.

Stovner, E.B., and Sætrom, P. (2019). epic2 efficiently finds diffuse domains in ChIP-seq data. Bioinformatics *35*, 4392–4393.

Su, S., Guntur, A.R., Nguyen, D.C., Fakory, S.S., Doucette, C.C., Leech, C., Lotana, H., Kelley, M., Kohli, J., Martino, J., et al. (2018). A Renewable Source of Human Beige Adipocytes for Development of Therapies to Treat Metabolic Syndrome. Cell Rep. *25*, 3215–3228.e9.

Swift, J., Ivanovska, I.L., Buxboim, A., Harada, T., Dingal, P.C., Pinter, J., Pajerowski, J.D., Spinler, K.R., Shin, J.W., Tewari, M., et al. (2013). Nuclear lamin-A scales with tissue stiffness and enhances matrix-directed differentiation. Science *341*, 1240104.

Tan, W.L.W., Anene-Nzelu, C.G., Wong, E., Lee, C.J.M., Tan, H.S., Tang, S.J., Perrin, A., Wu, K.X., Zheng, W., Ashburn, R.J., et al.; CHARGE-Heart Failure Working Group, CHARGE-EchoGen Consortium (2020). Epigenomes of Human Hearts Reveal New Genetic Variants Relevant for Cardiac Disease and Phenotype. Circ. Res. *127*, 761–777.

Taylor, M.R., Fain, P.R., Sinagra, G., Robinson, M.L., Robertson, A.D., Carniel, E., Di Lenarda, A., Bohlmeyer, T.J., Ferguson, D.A., Brodsky, G.L., et al.; Familial Dilated Cardiomyopathy Registry Research Group (2003). Natural history of dilated cardiomyopathy due to lamin A/C gene mutations. J. Am. Coll. Cardiol. *41*, 771–780.

Vergnes, L., Péterfy, M., Bergo, M.O., Young, S.G., and Reue, K. (2004). Lamin B1 is required for mouse development and nuclear integrity. Proc. Natl. Acad. Sci. USA *101*, 10428–10433.

Wen, B., Wu, H., Shinkai, Y., Irizarry, R.A., and Feinberg, A.P. (2009). Large histone H3 lysine 9 dimethylated chromatin blocks distinguish differentiated from embryonic stem cells. Nat. Genet. *41*, 246–250.

Worman, H.J. (2018). Cell signaling abnormalities in cardiomyopathy caused by lamin A/C gene mutations. Biochem. Soc. Trans. *46*, 37–42.

Worman, H.J., and Bonne, G. (2007). "Laminopathies": a wide spectrum of human diseases. Exp. Cell Res. *313*, 2121–2133.

Wu, W., Muchir, A., Shan, J., Bonne, G., and Worman, H.J. (2011). Mitogen-activated protein kinase inhibitors improve heart function and prevent fibrosis in cardiomyopathy caused by mutation in lamin A/C gene. Circulation *123*, 53–61.

Wu, S.Y., Lee, A.Y., Lai, H.T., Zhang, H., and Chiang, C.M. (2013). Phospho switch triggers Brd4 chromatin binding and activator recruitment for gene-specific targeting. Mol. Cell *49*, 843–857.

Xie, W., Chojnowski, A., Boudier, T., Lim, J.S., Ahmed, S., Ser, Z., Stewart, C., and Burke, B. (2016). A-type Lamins Form Distinct Filamentous Networks with Differential Nuclear Pore Complex Associations. Curr. Biol. *26*, 2651–2658.

Zheng, X., Hu, J., Yue, S., Kristiani, L., Kim, M., Sauria, M., Taylor, J., Kim, Y., and Zheng, Y. (2018). Lamins Organize the Global Three-Dimensional Genome from the Nuclear Periphery. Mol. Cell *71*, 802–815.e7.

Zhu, W.Z., Van Biber, B., and Laflamme, M.A. (2011). Methods for the derivation and use of cardiomyocytes from human pluripotent stem cells. Methods Mol. Biol. *767*, 419–431.

Zullo, J.M., Demarco, I.A., Piqué-Regi, R., Gaffney, D.J., Epstein, C.B., Spooner, C.J., Luperchio, T.R., Bernstein, B.E., Pritchard, J.K., Reddy, K.L., and Singh, H. (2012). DNA sequence-dependent compartmentalization and silencing of chromatin at the nuclear lamina. Cell *149*, 1474–1487.

STAR★METHODS

KEY RESOURCES TABLE

REAGENT or RESOURCE	SOURCE	IDENTIFIER
Antibodies		
Mouse monoclonal anti-Troponin T (flow cytometry)	Abcam	ab8295; RRID:AB_306445
Goat anti-mouse IgG Alexa 488 (flow cytometry)	ThermoFisher	A32723; RRID:AB_2633275
Rabbit polyclonal anti-MLC 2V (flow cytometry)	Protein Tech	10906-1-AP; RRID:AB_2147453
Goat anti-Rabbit IgG Alexa 555 (flow cytometry)	ThermoFisher	A32732; RRID:AB_2633281
Mouse monoclonal anti-CD105	Miltenyi Biotec	130-099-125; RRID:AB_2661357
Mouse monoclonal anti-CD73	Miltenyi Biotec	130-120-152; RRID:AB_2752016
Mouse monoclonal anti-CD90 (discontinued)	Miltenyi Biotec	130-097-935; RRID:AB_2660949
Mouse monoclonal anti-CD146	Miltenyi Biotec	130-097-939; RRID:AB_2660768
Rat monoclonal anti-AN2 (NG2)	Miltenyi Biotec	130-100-468; RRID:AB_2651231
Monoclonal anti-PDGFRβ (CD140b, discontinued)	Miltenyi Biotec	130-105-322; RRID:AB_2655084
Rabbit polyclonal anti-LAMIN B1	Abcam	ab16048; RRID:AB_443298
Goat polyclonal anti-LAMIN B (discontinued)	Santa Cruz	sc-6216; RRID:AB_648156
Mouse monoclonal anti-LAMIN A/C	Santa Cruz	Sc-376248; RRID:AB_10991536
Rabbit polyclonal anti-Histone H3	Abcam	ab1791;RRID:AB_302613
Mouse monoclonal anti-PAX6	DSHB	PAX6; RRID:AB_528427
Mouse monoclonal anti-GAPDH	Abcam	ab9484;RRID:AB_307274
Mouse monoclonal anti-ALBUMIN	Cedarlane Labs	CL2513A; RRID:AB_10086438
Goat polyclonal anti-NKX-5 (discontinued)	Santa Cruz	sc-8697;RRID:AB_650280
Goat polyclonal anti-SOX2 (discontinued)	Santa Cruz	sc-17320; RRID:AB_2286684
Mouse monoclonal anti-LHX2	DSHB	PCRP-Lhx2-2E3; RRID:AB_2722231
Mouse monoclonal H3K9me2 (ChIP)	Abcam	Ab1220; RRID:AB_449854
Rabbit polyclonal anti-H3K9me2 (immunofluorescence)	Active Motif	39239; RRID:AB_2793199
Goat polyclonal anti-HN4α (discontinued)	Santa Cruz	sc-6556;RRID:AB_2117025
Goat polyclonal anti-TNNT2 (immunofluorescence)	Sigma-Aldrich	SAB2502131;RRID:AB_2868459
Mouse monoclonal anti-TNNT2 (immunofluorescence)	ThermoFisher	MA5-12960; RRID: AB_11000742
Mouse monoclonal anti-TNNT2 (immunohistochemistry)	ThermoFisher	MS-295-p1;RRID:AB_61808
Donkey anti-Goat IgG Alexa 488	ThermoFisher	A11055;RRID:AB_2534102
Donkey anti-Rabbit IgG Alexa 488	ThermoFisher	A21206;RRID:AB_2535792
Donkey anti-Mouse IgG Alexa 488	ThermoFisher	A21202;RRID:AB_141607
Donkey anti-Rabbit IgG Alexa 568	ThermoFisher	A10042;RRID:AB_2534017
Donkey anti-Mouse IgG Alexa 568	ThermoFisher	A10037;RRID:AB_2534013
Donkey anti-Goat IgG Alexa 568	ThermoFisher	A11057;RRID:AB_142581
Donkey anti-Rabbit IgG Alexa 647	ThermoFisher	A31573;RRID:AB_2536183
Donkey anti-Mouse IgG Alexa 647	ThermoFisher	A31571;RRID:AB_162542
Donkey anti-Goat IgG Alexa 647	ThermoFisher	A21447;RRID:AB_141844
Goat anti-Mouse IgG HRP conjugated	Cell Signaling	7076;RRID:AB_330924
Goat anti-Rabbit IgG HRP conjugated	Cell Signaling	7074;RRID:AB_2099233
Biological samples		
Human cardiac tissue for immunohistochemistry and nuclei size quantification, IRB#802781	Margulies laboratory, Perelman School of Medicine, University of Pennsylvania	N/A
Chemicals, peptides, and recombinant proteins		
StemMACS IPS-Brew XF medium	Miltenyi Biotec	130-104-368
Plasmocin	InvivoGen	Ant-mpp

(*Continued on next page*)

Continued

REAGENT or RESOURCE	SOURCE	IDENTIFIER
Y-27632, ROCK inhibitor	Santa Cruz	sc-281642A
B-27 Supplement, minus insulin	ThermoFisher	A1895601
B-27 Supplement	ThermoFisher	17504044
Human/mouse/rat Activin A	R & D Systems	338-AC
Human BMP-4	R & D Systems	314-BP
CHIR 99021	Cayman Chemicals	13122
XAV939	Tocris	3748
Human BMP-4	Peprotech	120-05
Human FGF Basic	R & D Systems	233-FB
Human HGF	Peprotech	100-39
HCM Hepatocyte Culture Media	Lonza	CC-3198
Human Oncostatin M	R & D Systems	295-OM
STEMdiff Mesoderm Induction Medium	Stem Cell Technologies	05221
Mesencult-ACF Plus medium	Stem Cell Technologies	05448
IL-4 (human)	Peprotech	200-04
SB431542	Tocris	161410
EGM-2 Endothelial Cell Growth Medium-2 BulletKit (without FGF basic)	Lonza	CC-3162
IBMX (3-Isobutyl-1-methylxanthine)	Acros Organics	AC228420050
Dexamethasone	Sigma-Aldrich	D4902
Indomethacin	Sigma-Aldrich	I8280
T3 (3,3′,5-Triiodo-L-thyronine sodium salt)	Sigma-Aldrich	T6397
Insulin	Hospital of the University of Pennsylvania Pharmacy	N/A
Rosiglitazone maleate	Cayman Chemicals	11884
BODIPY 493/503	ThermoFisher	D3922
Flou-4, AM	ThermoFisher	F14201
DAPI	Sigma-Aldrich	D9542
Critical commercial assays		
NEB Ultra II DNA Library Prep Kit	New England Biolabs	E7645
NEBNext Poly(A) mRNA Magnetic Isolation Module	New England Biolabs	E7490
Deposited data		
Raw and analyzed ChIP-seq and RNA-seq data	This paper	GEO: GSE136252
Experimental models: cell lines		
IMR90 cells	ATCC	CCL-186 RRID:CVCL_0347
DiPS 1016 SevA hiPSC line	HSCI hIPSC core	DiPS 1016SevA RRID: CVCL_UK18
DiPS 1016 SevA hiPSC line, LMNA control lines	This study	N/A
DiPS 1016 SevA hiPSC line, LMNA T10I	This study	N/A
DiPS 1016 SevA hiPSC line, LMNA R541C	This study	N/A
Oligonucleotides		
LMNA T10I sgRNA oligo: 5′- GCTGGCCTGCGCCCCGCTGC-3′	This study	N/A
LMNA T10I repair template: 5′-CGCCCTTTCCGGGACCCCTGC CCCGCGGGCAGCGCTGCCAACCTGCCGGCCATGGAGACCC CGTCCCAGCGGCGCGCCATCCGCAGCGGTGCGCAGGCCAG CTCCACTCCGCTGTCGCCCACCCGCATCACCCGGCTGCAGG AGAAGGAGGACCTGCAGGAGCTCAATGA-3′	This study (IDT)	N/A
LMNA R541C sgRNA oligo: 5′-GGAAGTGGCCATGCGCAAGC-3′	This study	N/A

(*Continued on next page*)

Continued

REAGENT or RESOURCE	SOURCE	IDENTIFIER
LMNA R541C repair template: 5′-GTCACTGGGGTAGACATGCTGT ACAACCCTTCCCTGGCCCTGACCCTTGGACCTGGTTCCATGTCC CCACCAGGAAGTGGCCATGTGCAAGCTGGTGCGCTCAGTGACT GTGGTTGAGGACGACGAGGATGAGGATGGAGATGACCTGCTCC ATCACCACCACGTGAGTG – 3′	This study (IDT)	N/A
Recombinant DNA		
mEmerald-LaminA	Addgene	54139 RRID: Addgene_54139
mEmerald-LaminA-T10I	This study	NA
pGuide	Addgene	64711 RRID: Addgene_64711
pCas9-GFP	Addgene	44719 RRID: Addgene_44719
Software and agorithms		
Trimmomatic	Bolger et al., 2014	http://www.usadellab.org/cms/?page=trimmomatic
BWA Version 0.7.17	Li and Durbin, 2009	http://bio-bwa.sourceforge.net/
PicardTools	Open Source	http://broadinstitute.github.io/picard/
Deeptools Version 3.1.1	Ramírez et al., 2016	https://pypi.org/project/deepTools/
SAMtools	Li et al., 2009	http://samtools.sourceforge.net/
EDD	Lund et al., 2014	https://github.com/CollasLab/edd
BEDTools	Quinlan and Hall, 2010	https://code.google.com/p/bedtools
EPIC2	Stovner and Sætrom, 2019	https://github.com/biocore-ntnu/epic2
DiffBind	Stark and Brown, 2011	https://www.bioconductor.org/packages/release/bioc/html/DiffBind.html
GREAT	McLean et al., 2010	http://great.stanford.edupublic/html
Gprofiler	Raudvere et al., 2019	https://biit.cs.ut.ee/gprofiler/gost
R Stats Package	R Core Team, 2012	https://www.rdocumentation.org/packages/stats
Rsubread	Liao et al., 2019	https://bioconductor.org/packages/release/bioc/html/Rsubread.html
EdgeR	Robinson et al., 2010	http://bioconductor.org/packages/release/bioc/html/edgeR.html
Limma	Ritchie et al., 2015	http://bioconductor.org/packages/release/bioc/html/limma.html
PCATools	Blighe and Lun, 2019	https://github.com/kevinblighe
ComplexHeatmap	Gu et al., 2016	https://www.bioconductor.org/packages/release/bioc/html/ComplexHeatmap.html
bam-readcount	Open Source	https://github.com/genome/bam-readcount

RESOURCE AVAILABILITY

Lead contact

Further information and requests for resources and reagents should be directed to Rajan Jain (jainr@pennmedicine.upenn.edu).

Materials availability

Human iPSC-lines and plasmids generated in this study will be maintained within Musunuru and Jain laboratories. They will be supplied upon reasonable request and fulfillment of material transfer agreements, as appropriate.

Data and code availability

The ChIP-seq, RNA-seq, EDD peaks, and RNA expression matrices are available via GEO (GEO: GSE136252).

EXPERIMENTAL MODEL AND SUBJECT DETAILS

hiPSC Line Culturing

The DiPS 1016 SevA hiPSC line (1016, RRID: CVCL_UK18) was obtained from the Harvard Stem Cell Institute hiPSC Core Facility. Cells were grown under feeder-free conditions on Geltrex (Life Technologies)-coated plates in chemically defined StemMACS IPS-Brew XF medium (Miltenyi Biotec) supplemented with 1% penicillin/streptomycin and 5 μg/mL Plasmocin (InvivoGen). Medium was changed every 24 hours. At 80%–90% confluence, cells were dissociated with Accutase and split at a 1:8 ratio to create frozen stocks and working stocks that were maintained in culture.

Human Myocardial Studies

Failing and nonfailing human heart tissues were obtained from heart transplant recipients and brain-dead organ donors. *In situ* cardioplegia was employed for cardio protection in all human heart procurements, as previously described (Chen et al., 2018; Dipla et al., 1998). *In vivo* echocardiography was performed prior to harvest for contemporaneous assessment of *in vivo* structure and function. Procurement of human myocardial tissue was performed under protocols and ethical regulations approved by Institutional Review Boards at the University of Pennsylvania (IRB#802781) and the Gift-of-Life Donor Program (Pennsylvania, USA). In all cases, hearts were arrested *in situ* using ice-cold cardioplegia solution and transported on wet ice. Whole hearts and dissected left ventricle cavity were weighed to determine levels of hypertrophy. Transmural myocardial samples were dissected from the mid left ventricular free wall below the papillary muscle. Left ventricular tissues were taken for fixation in 4% paraformaldehyde (PFA); separate 1 g LV transmural tissue were flash frozen in liquid nitrogen for molecular assay within 4 h of explantation. For quantitation of nuclei size (Figure 1), nuclei from human myocardial images were stained with DAPI and anti-Tnnt2 (1:50, ThermoFisher MS-295-p1) and imaged on Keyence BZX710 (3 X 3 high powered fields were stitched together), and quantification was performed in ImageJ/FIJI. A median size filter was applied to the DAPI images (2.0 pixels) and the images were thresholded to highlight cardiomyocyte nuclei after a mask indicating Tnnt2+ signal was applied. The size of particles between 30-300 μm was quantified. The T10I patient referenced in this report presented with dilated cardiomyopathy, lipid abnormalities, and steatohepatitis of unclear etiology (patient 6.1 in Hussain et al., 2018). As relevant to the comparison of the comparison of the nuclei size of the proband indicated with comparators, cardiac status was classified as follows: non-failing donor hearts (with left ventricle ejection fraction greater than 50%) are further divided into normal and cHyp (Lang et al., 2006), as defined by an indexed left ventricular mass (left ventricular mass/body surface area) above 115 g/m^2 in men and 95 g/m^2 in women. Failing hearts with dilated left ventricular chamber size are classified as DCM, and failing hearts with ischemic injury are grouped as ICM. A proportion of the failing hearts manifest a combination of mixed etiology.

METHOD DETAILS

hiPSC Line Creation and Validation

For genome editing, control 1016 hiPSCs in a 60%–70% confluent 10-cm plate were dissociated with Accutase and resuspended a 0.4 cm cuvette with PBS containing pCas9-GFP plasmid, pGuide plasmid containing an LMNA-specific sgRNA (5′- GCTGGCCTGC GCCCCGCTGC-3′) and a single-stranded DNA oligonucleotide (IDT) LMNA T10I repair template— (5′ - CGCCCTTTCCGGGACCCC TGCCCCGCGGGCAGCGCTGCCAACCTGCCGGCCATGGAGACCCCGTCCCAGCGGCGCGCCATCCGCAGCGGTGCGCAGGCC AGCTCCACTCCGCTGTCGCCCACCCGCATCACCCGGCTGCAGGAGAAGGAGGACCTGCAGGAGCTCAATGA-3′). To generate the LMNA R541C iPSC line, the following were use: sgRNA, 5′-GGAAGTGGCCATGCGCAAGC-3′, and single-stranded DNA oligonucleotide (IDT) LMNA R541C repair template – (5′- GTCACTGGGGTAGACATGCTGTACAACCCTTCCCTGGCCCTGACCCTTGGA CCTGGTTCCATGTCCCCACCAGGAAGTGGCCATGTGCAAGCTGGTGCGCTCAGTGACTGTGGTTGAGGACGACGAGGATGAGG ATGGAGATGACCTGCTCCATCACCACCACGTGAGTG – 3′). A single pulse was delivered at 250 V/500 μF (Bio-Rad Gene Pulser), and the cells were recovered and plated in iPS-Brew with 5 μM ROCK inhibitor Y-27632, (Santa Cruz). After 48 hours, GFP positive cells were sorted and re-plated at limiting density into a 10 cm plate (such that only ~20 cells were in any plate). After 10 days, colonies were manually picked into individual wells of a 96-well plate. Hence, clones were derived from single cells. Once the wells reached 80%–90% confluence, cells were dissociated with Accutase and split at a 1:3 ratio to create a frozen stock and two working stocks that were maintained in culture. For genomic DNA isolation, cells were lysed in 50 μL lysis buffer (10mM Tris pH 7.5, 10mM EDTA, 10mM NaCl, 0.5% Sarcosyl) with 40 μg/mL Proteinase K overnight in a humidified incubator at 56°C. Genomic DNA was precipitated by addition of 100 μL 95% ethanol with 75mM NaCl, followed by incubation at –20°C for 2 hours. Precipitated DNA was washed three times with 70% ethanol, resuspended in 50 μL TE with 0.1 mg/mL RNase A, and dissolved at room temperature overnight. hiPSC clones were screened for correct mutation. Of 200 clones, four contained correct heterozygous knock-in alleles. At least two independent clonal lines were established for each genotype – T10I, R541C and control (lines that did not yield mutations) – and used for subsequent experimentation. All work in the study represents a combination of two clones per genotype.

hiPSC-Cardiomyocyte Differentiation

hiPSC-CMs were generated from hiPSCs adapting standard protocols. In brief, we used feeder-free differentiation conditions entailing the addition of a variety of growth factors and chemicals to the media. Undifferentiated hiPSCs were detached by a 4-min incubation with Accutase (STEMCELL Technologies) and seeded onto Geltrex (Life Technologies)-coated plates at 200,000 cells/cm2. To induce cardiac differentiation, we replaced hiPSC medium with RPMI/B27-insulin (RPMI-1640 with 2% B-27 Supplement Minus

Insulin; ThermoFisher Scientific) medium supplemented with recombinant human/mouse/rat activin A (100ng/mL; R&D Systems) for 18 hours, followed by recombinant human BMP-4 (5ng/mL; R&D Systems) and CHIR 99021 (1nM, Cayman Chemicals) for 2 days. The medium was then exchanged for RPMI/B27–insulin with XAV939 (1nM, Tocris) for another 2 days. The medium was then replaced with RPMI/B27–insulin without supplementary cytokines for three more days. RPMI-B27 (with insulin) was added every 2 to 3 days thereafter. Widespread spontaneous beating activity was typically observed 10-12 days after addition of activin A. hiPSC-CMs were chemically enriched at approximately day 20. Cells were collected at time points indicated.

Flow Cytometry

hiPSC-CMs were harvested and resuspended in 100μL cold PBS (2-4x10^6 cells/ml). 4% PFA was added to a final concentration 2%; cells were fixed on ice for 30 minutes and then washed twice with PBS. Cells were resuspended in 100μl of diluted Cardiac Troponin T primary antibody in PBS + 3% BSA (1:400, Abcam, ab8295) for 1 hour at room temperature. Cells were washed three times in PBS; cells were centrifuged at 400xg for 5 minutes between washes. Cells were resuspended in fluorochrome-labeled secondary antibody (goat anti-mouse IgG, 1:1000, ThermoFisher Scientific, A32723) diluted in PBS + 3% BSA and incubated for 30 min at room temperature. Control cells were incubated with secondary antibody only. Cells were washed as above, and resuspended in ice cold PBS, 3% BSA. Cells were analyzed using a BD Accuri flow cytometer. A similar protocol was followed for MLC2v flow cytometry, except Rabbit anti-MLC2v (Protein Tech, 10906-1-AP) and Goat anti-Rabbit secondary (ThermoFisher, A32732) were used.

Calcium Measurements

hiPSC-CMs were loaded with Fluo4 (ThermoFisher, F14201) at 1μM for 20 minutes at 37°C, ambient O_2 and 5% CO_2. Following media change, cells were allowed to equilibrate and de-esterize for 5 minutes at 37°C, ambient O_2 and 5% CO_2. Cells were stimulated at 2 Hz at 25V, a frequency and voltage designed to synchronize the autonomous beating of the dish. At 2Hz, most dishes synchronized to ~1-1.3Hz. For analysis purposes, no traces exceeding 1.5Hz were included in the average traces as this could confound the peak and rise/decay kinetic measurements. Calcium traces were acquired using a Zeiss 880 Airyscan confocal microscope operating on an Axiovert Z1 inverted microscope equipped with Plan-Apochromat 20x air 0.8 NA using a 488 line scan. For analysis, individual calcium traces were manually synchronized to the TTL pulse and averaged over 5 beats per cell to reduce beat-to-beat and signal noise. From those averages, the F0 was derived from the minimum value measured and the peak height from the peak height. Rise and decay parameters were derived from 0,1 normalization of the F/F0 trace.

Atomic Force Microscopy

Mechanical properties at the microscopic scale were measured using nanoindentation (Piuma; Optics11, Amsterdam, the Netherlands). A spherical indentation probe with a radius of 3.05 μm and a stiffness of 0.026 N/m was used. Cardiomyocytes were indented to a depth of 1–2 μm with velocities of 0.1, 0.25, 0.5, 1.0, 2.0, 5.0, 10.0, 20.0, 50.0, 100.0, and 150.0 μm/s. The tip was held in this indentation depth for 1 s and retracted over 1.5 s. The Young's moduli were calculated automatically by the software by fitting the force versus indentation curve to the Hertz equation. The Young's modulus E is derived from the fit of the initial 60% of the loading force-displacement curve (F(h)), the indenter tip (R), and indentation depth (h), according to the Hertz equation for a spherical indenter, for which a Poisson's ratio (ν) of 0.5 was assumed. $F(h) = (4/3)E(1-\nu 2)R1/2h3/2$

Fabrication of 3D Micropatterned Cardiac Cultures

hiPSC-CMs between day 30 and day 35 were dissociated using TrpLE Express (Sigma) and dispensed at a final cell density 1 × 10^6 cells/ml into each sterilized agarose replica molds. The 9 × 9 array agarose molds with spherical microwells were fabricated by pipetting 700μl of sterile molten agarose 2% ((w/v) in H_2O) *in silico*ne micro-molds (Microtissues Inc., Providence RI, US) and allowing them to gel in a biosafety cabinet for 15-20 mins. The replicas were then carefully transferred to a sterile 12-well plate by flexing the micro-mold, followed by sterilization under UV radiation for 60 mins. Each mold consisting of 81 microwells were washed three times with sterile PBS prior to cell seeding. hiPSC-CMs were counted and 200μl of the cell suspension was added to each mold in a dropwise manner. The cells were then allowed to settle into the microwells for two hours at 37°C and 5% CO2. After incubation, the micropatterned cardiac cultures were equilibrated by addition of 2ml of RPMI media supplemented with B27 Supplement (GIBCO) surrounding the agarose replica molds. Media was replaced around the molds every two days. hiPSC-CMs self-assembled into spontaneously beating micropatterned cultures 2-3 days after seeding.

Micropatterned Cardiac Culture Contractility Analyses

Phase contrast video recordings of the beating micropatterned cardiac cultures were captured at 30 frames per second (fps) on an Echo Revolve microscope using a 10X objective (Echo Laboratories, San Diego, US). The videos were exported as a series of multi-image stacks and analyzed using a motion tracking algorithm (Huebsch et al., 2015). The algorithm allows calculation of motion vector analyses by tracking the movement of block pixels from one frame to the other. Region of interest (ROI) were chosen to include the entire boundary of the beating micropatterned culture. The contraction and relaxation velocities were plotted as biphasic waveforms and annotated using the peak identification tool. The first peak was annotated as contraction and the second peak as relaxation. An average motion velocity heatmap was generated for each video based on pre-determined ROI tracings. Temporal information of absolute motion was detected as a mean of motion vectors along X and Y-axes.

Human Myocardial Gene Expression Analysis

For human myocardial gene expression analysis, the upregulated genes in *LMNA* mutant hearts compared to non-failing controls were obtained from GEO (GSE120836). All genes reported with log2 FC > |0.585| were included in analysis (2363 genes). Next, we identified a signature of genes upregulated in myocardium samples taken at the time of explant from patients with idiopathic dilated cardiomyopathy compared to non-failing donor controls from 89 and 122 patients, respectively (1353 genes, samples were collected by the Margulies and Cappola laboratories as part of an ongoing tissue bank at the University of Pennsylvania). Genes uniquely upregulated in *LMNA* mutant hearts were analyzed using Panther (GO-BP Slim Categories, Fisher's Exact Test with FDR correction). All categories identified in the analysis are reported in supplemental data. Genes from categories shown in Figure 6A were identified and combined into a single list and subsequently filtered for genes expressed in the hiPSC-CM datasets (n = 727 genes). Expression of genes from the LMNA mutant myocardium (n = 1715) or combined signature were categorized as upregulated, downregulated or not changed in the hiPSC d25 RNA-seq data (mutant compared to control, log2 FC $\geq$ |1.5|, FDR < 0.05). Changes in LB1 occupancy in hiPSC-CM datasets were calculated as described below using a 50kb window upstream or downstream of the TSS of each gene.

hiPSC-Hepatocyte Differentiation

Following established protocols (Cai et al., 2008), control, LMNA T10I, LMNA R541C hiPSCs were grown in feeder-free differentiation conditions. For efficient hepatocyte differentiation, cells were incubated in definitive endoderm media with recommended supplements (Stem Cell Technologies) for 4 days in ambient O_2 and 5% CO_2, yielding homogeneous monolayer of definitive endoderm cells. At day 5, cells were incubated with recombinant human BMP-4 (20ng/mL; Peprotech) and recombinant human FGF basic (10ng/mL; R&D Systems) for 5 days in RPMI-B27 (with insulin) in 5% O_2 and 5% CO_2, yielding hepatic progenitor cells. At day 10, cells were incubated in RPMI-B-27 (with insulin) supplemented with recombinant human HGF (20ng/mL; PeproTech) for 5 days at 5% O_2 and 5% CO_2, yielding immature HLCs. Finally, at d15, cells were incubated with HCM Hepatocyte Culture Medium (Lonza) without EGF and supplemented with recombinant human oncostatin M (20ng/mL; R&D Systems) for 7 days in ambient O_2 and 5% CO_2, yielding mature HLCs, which were collected at day 23 for subsequent ChIP, immunofluorescence, and immunoblotting.

hiPSC-Adipocyte Differentiation

Adipocyte differentiation was carried out following published method (Su et al., 2018) for generation of beige adipocytes from hiPSCs. Control, T10I and R541C hiPSCs were induced for mesoderm in STEMdiff Mesoderm Induction Medium (Stem Cell Technologies) for 4 days. On day 5, cells were incubated with Mesencult-ACF Plus medium (Stem Cell Technologies) to induce mesenchymal stem cell (MSC) formation. Media was refreshed daily from day 5 to day 12. Starting on day 12 and every 3 days thereafter until day 30, cells were passaged at 1:2 or 1:3 ratio in the same media and assayed at each passage for MSC surface markers CD105, CD73, CD90, and mural cell markers CD146, PDGFRβ and NG2 by flow cytometry. At day 30, when the cells were 95% positive for these markers, they were then plated on Animal Component-Free Cell Attachment Substrate (Stem Cell Technologies)-coated plates for adipocyte conversion. The following day, cells were incubated for 2 days in Mesencult ACF Plus media supplemented with human IL-4 (10nM) and the TGFβ inhibitor SB431542 (5 μM) to obtain adipocyte precursors. Cells were then induced for adipogenesis for 3 days in EGM-2 media without FGF basic (Lonza) supplemented with adipogenic induction cocktail (0.5mM IBMX, 5uM dexamethasone, 125 μM indomethacin, 2nM T3, 170nM insulin, 1 μM rosiglitazone, and 5 μM SB31542). Finally, cells were maintained in EGM-2 without FGF basic supplemented with only insulin, T3, rosiglitazone and SB431542 until adipogenesis is complete. Adipocytes were harvested on day 14-20 for subsequent analyses.

Protein Isolation and Immunoblot Analysis

Total protein was isolated in cold RIPA (150mM NaCl, 1% NP-40, 0.5% Na deoxycholate, 0.1% SDS, 50mM Tris-HCl pH 8.0) with protease inhibitors, boiled for 10 minutes at 100°C and pulse sonicated. Lysate was cleared with addition of Triton X-100 to final 1% and centrifugation at 4°C for 10 minutes at 20000xg in microcentrifuge; for hiPSC-adips, cleared lysate was spun a second time (4°C for 10 minutes at 20000xg in microcentrifuge) and any visible lipid at the top of the supernatant was removed by manual micropipetting. 30ug total protein (with addition of 1mM DTT and 1x sample loading buffer) was run on 4%–12% Bis-Tris protein gels (Invitrogen #NP0335), transferred to PVDF, and blocked in 5% milk in 1xTBS-T for 1 hour at room temperature with agitation. Blots were probed at room temperature with agitation using antibodies for: LAMIN B1 (1:1000 ab16048; abcam), LAMIN A/C (1:200 sc-376248; Santa Cruz), Histone H3 (1:1500 ab1791; abcam), PAX6 (1:500 DSHB), GAPDH (1:2000 ab9485 abcam), ALBUMIN (1:1000 CL2513A; Cedarlane Labs). Secondary antibody binding was performed at room temperature with agitation using: anti-rabbit HRP-conjugated IgG antibody or anti-mouse HRP-conjugated IgG antibody (1:3000 7074, 7076; Cell Signaling) at 1:3000. Extensive washes (~10 washes in 1 hour) were performed following primary and secondary antibody using 1xTBS-T. Visualization was achieved using Pierce ECL Plus (ThermoFisher) or SuperSignal West Femto Chemiluminescent Substrate (ThermoFisher). No blots shown were stitched together.

Immunofluorescence

Control, LMNA T10I, and LMNA R541C hiPSC-CMs, -heps, and -adips were grown and differentiated on ibidi μ-Slide 8 well glass bottom chambers (Ibidi cat#80827) or glass coverslips, fixed with 4% paraformaldehyde (PFA) for 10 minutes at room temperature, permeabilized with 0.25% Triton X-100 for 10 minutes, blocked in 1% BSA in PBS-T (8mM Na_2HPO_4, 150mM NaCl, 2mM KH_2PO_4,

3mM KCl, 0.05% Tween 20, pH 7.4) and incubated with primary and secondary antibodies diluted in PBS-T + 1% BSA for 1 hour each at room temperature. Samples were counterstained with DAPI solution (Sigma, cat#D9542) for 10 minutes at room temperature, then rinsed with PBS and stored/imaged in 80% glycerol mounting media (80% glycerol, 0.1% sodium azide, 0.5% propyl gallate, 20mM Tris-HCl, pH 8.0).

Primary antibodies included: Lamin B1 (1:750 ab16048; Abcam), Lamin B (1:500 sc-6216, Santa Cruz), LAMIN A/C (1:200 sc-376248, SantaCruz), NKX2-5 (1:1000 sc-8697, Santa Cruz), TNNT2 (1:500 MA512960; ThermoFisher), PAX6 (1:10 DSHB), SOX2 (1:250, sc-17320; Santa Cruz), LHX2 (1:10 PCRP-LHX2-2E3, DSHB), H3K9me2 (1:1000 Active Motif, 39239), HNF4α (1:500, sc-6556, Santa Cruz), TNNT2 (1:100 SAB2502131, Sigma). Secondary antibodies included: Donkey anti-Goat Alexa 488 (1:1000 A11055, ThermoFisher); Donkey anti-Rabbit Alexa 488 (1:1000 A21206; ThermoFisher), Donkey anti-Mouse Alexa 488 (1:1000 A21202; ThermoFisher), Donkey anti-Rabbit Alexa-568 (1:1000 A10042; ThermoFisher), Donkey anti-Mouse Alexa-568 (1:1000 A10037; ThermoFisher), Donkey anti-Goat Alexa-568 (1:1000 A11057, ThermoFisher), Donkey anti-Rabbit Alexa-647 (1:1000 A31573; ThermoFisher), Donkey anti-Mouse Alexa-647 (1:1000 A31571; ThermoFisher), Donkey anti-Goat Alexa 647 (1:1000, A21447; ThermoFisher). All cells used for nuclear morphology quantification were stained with LAMIN B1, LAMIN B, and /or LAMIN A/C antibodies. BODIPY 493/503 (4,4-Difluoro-1,3,5,7,8-Pentamethyl-4-Bora-3a,4a-Diaza-*s*-Indacene; ThermoFisher) was used per manufacturer's recommendations (1 μM final) for lipid droplet assessment in hiPSC-adips.

All confocal immunofluorescent images of hiPSC-cell types were taken using a Leica TCS SP8 3X STED confocal microscope or Leica TCS SP8 and deconvoluted using Huygens Professional software. DAPI staining (blue channel) were acquired using a PMT detector with offset $-$0.1%. All other fluorescent staining (green, red and far red channels) were acquired using HyD detectors in the standard mode with 100% gain. Images were taken as Z stacks with 0.05-0.1 μm intervals with a range of 10-50 Z-planes per image. Representative confocal images of hiPSC-cell types show a single focal plane. Image analysis was performed using ImageJ software (National Institute of Health, USA). Measurement of localization of the IF signal at the nuclear periphery was performed as a proportion of the signal at the nuclear periphery to total signal in the nucleus. Nuclear periphery and whole nucleus regions of interest (ROIs) were created with signal threshold tool on default parameters using DAPI or nuclear lamina/ H3K9me2 signals, respectively. BODIPY stain imaging was performed on Leica THUNDER Imager 3D Cell Culture system with Thunder computational clearing workstation and DMi8 inverted microscope; max projection images from a stack of images were used for quantification of BODIPY and DAPI area.

ChIP and ChIP-seq Library Preparation

ChIP

hiPSC-CMs, hiPSC-heps, and hiPSC-adips were crosslinked in culture by addition of methanol-free formaldehyde (ThermoFisher, final 1% v/v) and incubated at room temperature for 10 minutes with gentle rotation. Crosslinking was quenched by addition of glycine (final 125mM) and incubated at room temperature for 5 minutes with gentle rotation. Media was discarded and replaced with PBS; cells were scraped and transferred to conical tubes and pelleted by centrifugation (250xg, 5 minutes at room temperature). Resulting pellets were flash frozen on dry ice and stored at $-$80C.

For ChIP, 30μL protein G magnetic beads (per ChIP sample; ThermoFisher) were washed 3 times in blocking buffer (0.5% BSA in PBS); beads were resuspended in 250μL blocking buffer and 2μg antibody (LAMINB1, Abcam, ab16048; H3K9me2, Abcam, ab1220) and rotated at 4°C for at least 6 hours. Crude nuclei were isolated from frozen crosslinked cells as follows: cell pellet (from 10cm plate) was resuspended in 10mL cold Lysis Buffer 1 (50mM HEPES-KOH pH7.5, 140mM NaCl, 1mM EDTA, 10% Glycerol, 0.5% NP-40, 0.25% Triton X-100, and protease inhibitors), and rotated at 4°C for 10 minutes, followed by centrifugation (250xg, 5 minutes at room temperature). Supernatant was discarded and the pellet was resuspended in 10mL cold Lysis Buffer 2 (10mM Tris-HCl pH 8.0, 200mM NaCl, 1mM EDTA, 0.5mM EGTA, and protease inhibitors), and rotated at room temperature for 10 minutes, followed by centrifugation (250xg, 5 minutes at room temperature). Supernatant was discarded and nuclei were resuspended/lysed in 1mL cold Lysis Buffer 3 (10mM Tris-HCl, pH 8.0, 100mM NaCl, 1mM EDTA, 0.5mM EGTA, 0.1% Na-Deoxycholate, and protease inhibitors) and transferred to pre-chilled 1mL Covaris AFA tubes (Covaris) Samples were sonicated using a Covaris S220 sonicator (high cell chromatin shearing for 15 minutes; Covaris). Lysates were transferred to tubes and Triton X-100 was added (final 1%) followed by centrifugation (top speed, 10 minutes at 4°C in microcentrifuge). Supernatant was transferred to a new tube; protein concentration was measured by Bradford assay. Antibody-conjugated beads were washed 3 times in blocking buffer, resuspended in 50μL blocking buffer and added to 500μg input protein for overnight incubation with rotation at 4°C. 50μg lysate was aliquoted and stored at $-$20C for input. On day 2, beads were washed 5 times in 1mL RIPA buffer (50mM HEPES-KOH pH 7.5, 500mM LiCl, 1mM EDTA, 1% NP-40, 0.7% Na-Deoxycholate) with 2-minute incubation at room temperature with rotation for each wash. Beads were washed in 1mL final wash buffer (1xTE, 50mM NaCl) for 2 minutes with rotation at room temperature before final resuspension in 210μL elution buffer (50mM Tris-HCl pH 8.0, 10mM EDTA, 1% SDS). To elute, beads were incubated with agitation at 65°C for 30 minutes. 200μL eluate was removed to a fresh tube, and all samples (ChIP and reserved inputs) were reverse-crosslinked overnight at 65C with agitation for a minimum of 12 hours, but not more than 18 hours. 200μL 1xTE was added to reverse crosslinked DNA to dilute SDS, and samples were RNaseA treated (final 0.2mg/mL RNase; 37°C for 2 hours) and Proteinase K (final 0.2mg/mL Proteinase K; 55°C for 2 hours) before phenol:chloroform extraction and resuspension in 10mM Tris-HCl pH 8.0.

Library Preparation

ChIP and input DNA were quantified by Qubit (ThermoFisher) before library preparation using the NEBNext Ultra II DNA library prep kit (NEB). Samples were indexed for multiplex sequencing. Library quality was analyzed by BioAnalyzer (Agilent Genomics) and

quantified using qPCR (Kapa Biosystems). Libraries were pooled for multiplex sequencing, re-quantified, and sequenced on the Illumina NextSeq500 platform (vII; 75bp single-end sequencing; high output; Illumina).

RNA Isolation and RNA-seq Library Preparation

Cells were isolated at indicated times, scraped from plates with 1xPBS, and centrifuged at 1500 g for 5 minutes at room temperature. After discarding supernatant, cell pellets were flash frozen in dry ice and stored at −80°C until processing. RNA was isolated using QIAGEN RNeasy total RNA extraction kit (QIAGEN). RNA quality was analyzed by BioAnalyzer; samples with RIN scores > 8 were chose for further processing. RNA libraries were prepared using the NEBNext Ultra II DNA Library Prep kit (NEB) with the NEBNext Poly(A) mRNA Magnetic Isolation Module (NEB) to enrich for poly-A tailed RNA molecules. RNA-seq library quality was analyzed by BioAnalyzer (Agilent Genomics) and quantified using qPCR (Kapa Biosystems). Libraries were pooled for multiplex sequencing, re-quantified, and sequenced on the Illumina NextSeq500 platform (vII; 75bp single end sequencing; high output; Illumina).

ChIP-seq Analysis

Alignment and Processing

Raw reads were trimmed with Trimmomatic v0.32 and then aligned to hg19 genome using bwa (Version 0.7.17) aln with parameters 'bwa aln -q 5 -l 32 -k 2′. Bwa samse was then used to convert to sam format. Sam files were then filtered using samtools (version 1.7) view with '-F 1804 -q 30' parameters, sorted and converted to bam format. PCR duplicates were removed using Picardtools MarkDuplicates. All ChIP-seq libraries were downsampled to 14.2 million uniquely mapped aligned reads using samtools view with the -s flag. Replicate bigwig coverage tracks were made using Deeptools (version 3.1.1) bamCoverage with '—normalizeUsing RPGC -e 200' and hg19 blacklist. Spearman correlations of ChIP-seq libraries were computed via Deeptools 'multiBigWigSummary' using 100kb bins genome wide and plotted using 'plotCorrelation'. Samtools merge was used to combine biological replicate bam files into treatment bam files. Deeptools bamCoverage was used to make treatment bigwig files, which were then input into Deeptools bigWigCompare, creating input normalized bigwig coverage tracks for each treatment. log2 transformed tracks are shown. For all ChIP-seq data, replicates per genotype (control, T10I, and R541C) and cell type (hiPSC-CM d25 and d45, hiPSC-hep, and hiPSC-adip) were merged into a union dataset for LAD and KDD analysis following replicability measure (see below); GREAT analysis was performed using Epic2 peaks using individual data (see below). At least three replicates for control and T10I hiPSC-CMs at day 25 and d45 were merged for both LB1 and H3K9me2. Given the high correlation between R541C hiPSC-CM LB1 replicates and H3K9me2 replicates, ChIP-seq datasets from day 45 (replicates 1 and 2) and day 25 (replicate 1) were merged, to meet the minimum three replicate standard for the hiPSC-CM. For hiPSC-adips and hiPSC-heps, two replicates for control, R541C and T10I were merged per genotype and ChIP.

EDD

LADs and KDDs were called using EDD (version 1.1.18) (Lund et al., 2014) with paired merged ChIP and Input bam files, parameters '-bin-size auto -g 4–fdr 0.05', modified parameter config file 'required_fraction_of_informative_bins = 0.98' and hg19 blacklist. Bed files were clipped for chromosome ends using bedClip. LAD/KDD PCA analysis was performed using princomp function in R's stats package. LAD/KDD overlap assessments (by genome coverage) were performed using bedtools.

Contact Frequency and Gene Overlap

To calculate LAD normalized contact frequency, coverage tracks were parsed using multiBigwigSummary with '–outRawCounts' and LAD bed files. For Figure 4B, n = 1201 and 1333 total LAD regions for days 25 and 45, respectively; these regions represent the sections of control hiPSC-CMs LADs that are shared with T10I and/or present only in control. In Figure 4C, gene density analysis includes only LADs with at least one gene present; n = 640 and 753 total LAD regions for days 25 and 45, respectively A similar method was used to obtain enrichment around protein coding gene TSS regions by using a TSS ± 50kb window bed file. ChIP-seq contact frequency data from R541C (Figure S5D) was scaled to match control, since the sequencing was performed separately. Scaling of R541C tracks were performed using deeptools with a scale factor. Scale factor was the ratio of enrichment in the shared LAD regions between R541C and control treatments. For gene density assessments (Figures 4C and S5E) and to create all LAD gene lists (Table S1), genes overlap (minimum 1bp) was performed with bedtools using input LAD/KDD bed files (parsed as shared, control-only, or T10I/R541C-only). For density assessments, the total number of overlapping genes per feature was represented as a ratio of total genes/region size (bp).

Permutation Test

To test if T10I-only or R541C-only hiPSC-CM LADs are overrepresented in hiPSC-hep LADs (Figures 4F and S5G) we input T10I-only or R541C-only LADs into bedtools shuffle and exclude hg19 blacklist regions to randomly sample the hg19 genome using regions of the same size as the T10I-only or R541C-only hiPSC-CM LADs. This sampling was performed 1000 times; for each random sampling, we intersected the sample set against control hiPSC-CM LADs and calculated the genome coverage percentage of overlapping regions. Overlap percentages were built into a distribution, tested for normality via Shapiro test (for T10I: p value = 0.729; for R541C: p value = 0.531), and statistical significance was calculated two tailed one sample t test using the percent genome coverage of overlapping T10I-only or R541C-only hiPSC-CM LADs with control hiPSC-hep LADs as the true value of the mean (for T10I: 5.37761%; for R541C: 8.33403%).

DiffBind and GREAT

Peaks for differential binding analysis (used for GREAT in Figures 5 and S7) were called using Epic2 (Stovner and Sætrom, 2019) (version 0.0.16) with paired replicate ChIP and Input bam files, and parameters '-fs 200 -bin 600 -g 4 -fdr 0.05'. Resulting peak files,

along with paired replicate ChIP and Input bam files, were input into DiffBind (Ross-Innes et al., 2012; Stark and Brown, 2011) for differential binding analysis using FDR < 0.1 as significance threshold. Figure S7D displays genes that are within a 25kb window of DiffBind-identified regions and those which have altered expression (as defined by log2 fold change $\geq |1|$ and FDR < 0.05) are color coded based on expression. Differentially gained and lost peaks were input to GREAT web tool (McLean et al., 2010) web with default settings. Number of unique genes in each category derived from individual GREAT terms: 32, 21, 67, 26, 113, 103, 108, and 203 cell fate, endoderm, epithelium, inductive signaling, metabolism, neuron, other, and total unique list, respectively. Only those genes expressed in hiPSC-CM datasets were considered in analysis shown in Figure 5H (n = 172 in total). Gene lists from lost regions were analyzed using gProfiler webtool (Raudvere et al., 2019) (Table S4). Neurobiology gene list (Figure 5B) is comprised of the entire Brain Development Gene Ontology list (GO:0007420). Genes were considered LAD genes for this analysis if TSS was within 50 kb upstream or downstream of EDD-defined LAD. LB1 contact frequency was determined as described above.

RNA-seq Analysis

Raw reads were trimmed with Trimmomatic v0.32 and then aligned to hg19 genome using STAR (Dobin et al., 2013) (version 2.6.0c) and then filtered using samtools view with '-F 4 -q 10' parameters. Rsubread (Liao et al., 2019) featureCounts quantified the number of reads per feature of Ensembl hg19 gene annotation file. For differential gene expression analysis, genes with < 1 count per million (CPM) in less than 25% of samples were removed from differential expression analysis. For analyses using all genes, no cpm filter was applied. EdgeR's calcNormFactors (McCarthy et al., 2012; Robinson et al., 2010) was used to calculate library size normalization factors. Limma (Ritchie et al., 2015) voom function was used to log2 transform the CPM matrix. For differential expression analysis, Limma lmFit, contrast.fit and eBayes functions were used to fit the linear model, compute coefficients and standard error, and then perform differential expression calculation with Benjamini–Hochberg multiple correction adjusted P values (Benjamini and Hochberg, 1995). Cutoffs of FDR ≤ 0.05 and log2 fold change ≥ 1.5 or ≤ -1.5 were used for differentially upregulated or downregulated genes. RNA-seq PCA plots were created using PCAtools (https://github.com/kevinblighe) pca and biplot commands unless otherwise indicated. RNA-seq Heatmaps were made using ComplexHeatmap (Gu et al., 2016) package. bam-readcount (https://github.com/genome/bam-readcount) was used to count nucleotides at mutant positions for each RNA-seq library (Figures S1E and 2G). One T10I hiPSC-CM library (#303 – see GEO) was an outlier on PCA plot and could not be verified to be mutant (indicated by *) and hence was excluded from further analysis. All reported RNA-seq replicates were from d25 hiPSC-CMs.

QUANTIFICATION AND STATISTICAL ANALYSIS

Statistical details, including sample size/number of replicates, and details of what is plotted (mean versus median and SD or SEM) can be found in figure legends. Datasets were tested for normality prior to testing for significance and figure legends include the exact test used to assess significance. No strategies were employed regarding sample size or randomization of the data, unless otherwise indicated. Significance was defined as $p < 0.05$ unless otherwise indicated.